Mott Transitions and *d*-Wave Superconductivity in Half-Filled-Band Hubbard Model on Square Lattice with Geometric Frustration

Hisatoshi YOKOYAMA*, Masao OGATA[1] and Yukio TANAKA[2]

Department of Physics, Tohoku University, Sendai 980-8578
[1]*Department of Physics, University of Tokyo, Bunkyo-ku, Tokyo 113-0033*
[2]*Department of Applied Physics, Nagoya University, Nagoya 464-8603*

Mechanisms of Mott transitions and $d_{x^2-y^2}$-wave superconductivity (SC) are studied in the half-filled-band Hubbard model on square lattices with a diagonal hopping term (t'), using an optimization (or correlated) variational Monte Carlo method. In the trial wave functions, a doublon–holon binding effect is introduced in addition to the onsite Gutzwiller projection. We mainly treat a *d*-wave singlet state and a projected Fermi sea. In both wave functions, first-order Mott transitions without direct relevance to magnetic orders occur at $U = U_c$, which is approximately the bandwidth, for arbitrary t'/t. These transitions originate in the binding or unbinding of a doublon to a holon. *d*-wave SC appears in a narrow range immediately below U_c. The robust *d*-wave superconducting correlation is necessarily accompanied by enhanced antiferromagnetic correlation; the strength of SC decreases, as t'/t increases.

1. Introduction

In connection with the superconductor–insulator transitions in organic compounds κ-(BEDT-TTF)X,[1] the half-filled-band Hubbard model on anisotropic triangular lattices [Fig. 1(b)][2] has been intensively studied. In addition, a recent experimental study[3] has reported that a series of film samples of nondoped high-T_c cuprates (parent materials of electron-doped systems) do not become antiferromagnetic (AF) insulators but exhibit metallic properties including superconductivity (SC) at 21 K. Thus, it is important to grasp the mechanisms of Mott transitions and SC, if any, in half-filled-band Hubbard models with frustration. Because such phenomena arise at intermediate correlation strength ($U \sim W$; W being the bandwidth), one has to use a method that can reliably treat both strongly correlated and weakly correlated regimes. As one of such methods, the optimization (or correlated) variational Monte Carlo (VMC) method[4] has rapidly progressed in recent years for the study of ground-state properties.[5]

Using this method, the present authors have recently studied the Hubbard model on the anisotropic triangular lattice [Fig. 1(b)].[6] With a projected *d*-wave singlet state, it is found that (1) a conductive-to-nonmagnetic-insulator (Mott) transition occurs at $U = U_c$, which is somewhat smaller than W, and is caused by the binding (and unbinding) of a doublon to a holon; (2) $d_{x^2-y^2}$-wave SC appears in the vicinity of both the Mott transition and the AF phase, and develops together with the short-range AF correlation (or fluctuation).

In weakly frustrated cases, the two lattices in Figs. 1(a) and 1(b) have a common characteristic wave number $\mathbf{G} = (\pi, \pi)$ in spin correlation. In strongly frustrated cases, however, the characteristic wave numbers become different; for instance, 120°-structure spin correlation is probably
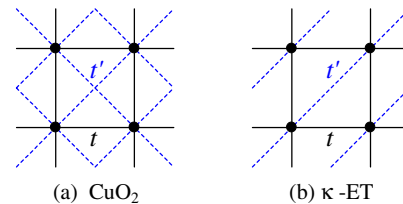

Fig. 1. (Color online) Lattice structure and hopping integrals t and t', (a) studied in this work, and (b) often used for κ-BEDT-TTF salts. Lattice sites are denoted by dots.

dominant in (b) for $t' \sim t$,[7] whereas the collinear structure is favored in (a). In this paper, we carry out similar detailed calculations for the lattice, often treated in the context of high-T_c cuprates (t–t'–U model) [Fig. 1(a)], and reveal whether or not the above mechanisms of the Mott transition and of SC also work here. In addition to the *d*-wave singlet state, we study Mott transitions in the projected Fermi sea.

The organization of this paper is as follows: In §2, we introduce the model and method we use. In §3 and §4, we discuss Mott transitions in the *d*-wave singlet state and in the projected Fermi sea, respectively. Section 5 is assigned to the stability and properties of the *d*-wave superconducting (SC) state. In §6, we construct a ground-state phase diagram based on the present VMC calculations, and address important problems with respect to antiferromagnetism (AF). In §7, we briefly summarize the main results and discuss the subject further.

Part of the present results have been reported in a previous letter.[8]

2. Model and Method

In §2.1, the model we study is introduced, and related studies are summarized. In §2.2, we briefly review the background of variational wave functions for the Hubbard model in the research on the Mott transition. In §2.3, we give

*E-mail: yoko@cmpt.phys.tohoku.ac.jp

an account of the wave functions used in this paper and the conditions of VMC calculations.

2.1 Hubbard model on frustrated square lattices

In this paper, we study the Hubbard model[9–11] on a square lattice with diagonal transfer t' [Fig. 1(a)],

$$\mathcal{H} = \mathcal{H}_{\mathrm{kin}} + \mathcal{H}_U = \sum_{\mathbf{k}\sigma} \varepsilon(\mathbf{k}) c_{\mathbf{k}\sigma}^\dagger c_{\mathbf{k}\sigma} + U \sum_j n_{j\uparrow} n_{j\downarrow}, \quad (1)$$

$$\varepsilon(\mathbf{k}) = -2t(\cos k_x + \cos k_y) - 4t' \cos k_x \cos k_y, \quad (2)$$

with $U, t > 0$. Equation (1) has been often used as a simple model that captures the essence of cuprates.[12] Here, we concentrate on the half-filled band ($n = N_{\mathrm{e}}/N_{\mathrm{s}} = 1$; N_{e}: electron number and N_{s}: site number) and consider doped cases in a forthcoming publication. We exclusively treat the case of $t' \leq 0$, because the behavior for t' (> 0) is identical to that for $-t'$, owing to the particle–hole symmetry at $n = 1$. Note that the negative sign of t'/t is in agreement with the hole-doped case of high-T_{c} cuprates. When $|t'/t|$ is varied, the features of the bare band, eq. (2), abruptly change at $|t'/t| = 0.5$, at which low-lying energy levels become strongly degenerate; the van Hove singularity points depart from $(\pi, 0)$ and $(0, \pi)$ for $|t'/t| > 0.5$. Furthermore, the plausible values of high-T_{c} cuprates are considered to be $|t'/t| = 0.1$–0.3.[13] Thus, we restrict the range of frustration strength to $0 \leq |t'/t| \leq 0.5$ in this paper.

Despite the importance of the model, reliable knowledge is limited, particularly in the intermediate and strong coupling regimes. For the pure square lattice ($t' = 0$), it is believed that the ground state is insulating with a long-range AF order for $U > 0$, owing to the complete nesting condition.[14] For frustrated cases ($t' \neq 0$), however, it is urgently required to clarify the properties of the conductor-insulator transition.[15–18] For SC at half filling, although the anisotropic triangular lattices have often been studied,[19] studies on the present lattice are rare to our knowledge.

2.2 Historical background of wave functions

As a many-body trial wave function, the Jastrow type[20] is useful and has been often applied: $\Psi = \mathcal{P}\Phi$, where $\mathcal{P}$ denotes a many-body correlation (Jastrow) factor composed of projection operators, and Φ is a one-body wave function usually given by a Slater determinant. For the Hubbard model, more than four decades ago, Gutzwiller introduced the celebrated onsite projection,[11]

$$\mathcal{P}_{\mathrm{G}} = \prod_j [1 - (1 - g) n_{j\uparrow} n_{j\downarrow}], \quad (3)$$

which has primary importance for arbitrary parameters in the Hubbard model. Although the Gutzwiller wave function (GWF), $\Psi_{\mathrm{G}}^{\mathrm{FS}} = \mathcal{P}_{\mathrm{G}} \Phi_{\mathrm{F}}$ (Φ_{F}: Fermi sea), looks simple, it is generally difficult to accurately calculate expectation values using it. Hence, a mean-field-type approximation [now called a Gutzwiller approximation (GA)] was introduced by Gutzwiller himself,[21] and was used and extended by many researchers for the following two decades.[22] However, variation theory loses its various advantages when additional approximations such as GA are applied, and consequently it becomes difficult to improve the wave function. To break this deadlock, VMC methods[23] have been applied to this problem;[24,25] thereby and by subsequent exact analytic

treatment in one dimension,[26] the precise behavior of $\Psi_{\mathrm{G}}^{\mathrm{FS}}$ was clarified for the first time. Although $\mathcal{P}_{\mathrm{G}}$ is indispensable for treating the Hubbard model, its independent use leads to the following physically unsatisfactory results: (1) The momentum distribution function $n(\mathbf{k})$ tends to be an increasing function of $|\mathbf{k}|$, (2) $2k_{\mathrm{F}}$ anomalies in the spin [charge density] structure factor $S(\mathbf{q})$ [$N(\mathbf{q})$] cannot be properly represented, and (3) a Mott transition cannot be described, in addition to the problem of a considerably high variational energy.

Although the electron–electron interaction in the Hubbard model is limited to within a single site, its effect reaches distant sites. Therefore, to overcome the above shortcomings of $\mathcal{P}_{\mathrm{G}}$, one needs to add intersite correlation (long-range Jastrow) factors. In cases of low electron density, distance-dependent long-range Jastrow factors are useful.[27] On the other hand, at half filling, the short-range part of the Jastrow factor is predominant owing to the screening effect. Castellani *et al.*[28] derived an effective Hamiltonian of the Hubbard model, taking account of both spin and charge degrees of freedom. In their effective Hamiltonian, an exchange term between a doubly occupied site (doublon) and an empty site (holon) appears, indicating that a doublon–holon correlation is inherent in the Hubbard model. Kaplan *et al.*[29] actually showed by studying one-dimensional (1D) small clusters that the binding of a doublon to a holon is important for large U/t to reduce the energy at half filling. Using exact diagonalization, Yokoyama and Shiba[27] studied the ground-state wave function of Hubbard rings at half filling, at which the ground state is known to be insulating for $U/t > 0$.[30] They found that, for large U/t, the magnitudes of the coefficients of bases with one doublon (and one holon) decrease exponentially as a function of the distance between doublon and holon. This means that a doublon is bound to a holon within the decay distance in an insulating state.

A simplified wave function that reflects the above arguments is written as $\Psi_Q = \mathcal{P}_Q \mathcal{P}_{\mathrm{G}} \Phi$.[27,29] Here, the doublon–holon binding factor $\mathcal{P}_Q$ is limited to the nearest-neighbor part:

$$\mathcal{P}_Q = \prod_i (1 - \mu Q_i^\tau), \quad (4)$$

$$Q_i^\tau = \prod_\tau [d_i(1 - e_{i+\tau}) + e_i(1 - d_{i+\tau})], \quad (5)$$

where $d_i = n_{i\uparrow} n_{i\downarrow}$, $e_i = (1 - n_{i\uparrow})(1 - n_{i\downarrow})$, and τ varies over all the nearest neighbors. A variational parameter μ ($0 \leq \mu \leq 1$) controls the strength of doublon–holon binding in the nearest-neighbor sites; as μ increases, a doublon tends to adhere to a holon, and for $\mu \to 1$, a doublon cannot leave a holon, as shown in Fig. 2.

This Jastrow factor, $\mathcal{P}_Q \mathcal{P}_{\mathrm{G}}$, can also be derived naturally from the strong-coupling expansion. It is known that the GWF with $g = 0$ is an extremely good trial state for the 1D Heisenberg model,[25,31] and that the Gutzwiller-type functions, $\mathcal{P}_{\mathrm{G}} \Phi_{\mathrm{AF}}$ and $\mathcal{P}_{\mathrm{G}} \Phi_{\mathrm{BCS}}$ (Φ_{AF}: Hartree–Fock-type AF state; Φ_{BCS}: $d_{x^2-y^2}$-wave BCS state), yield quantitatively reasonable results for the 2D t–J model.[32–34] These favorable properties of the GWF for strong-coupling models can be applied to the Hubbard model by considering a canonical transformation, $\mathcal{H}_{t-J} \sim \mathrm{e}^{\mathrm{i}S} \mathcal{H}_{\mathrm{Hub}} \mathrm{e}^{-\mathrm{i}S}$ ($t/U \to 0$),[35] and similarly,

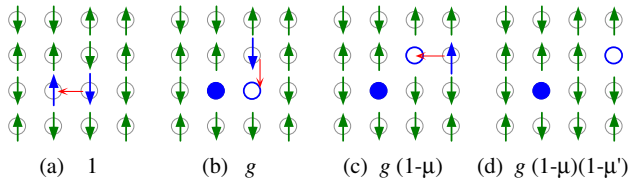(a) 1   (b) *g*   (c) *g* (1-μ)   (d) *g* (1-μ)(1-μ')

Fig. 2.   (Color online) Weight assignment of Jastrow factor $\mathcal{P} = \mathcal{P}_Q \mathcal{P}_G$ depending on local electron configuration. Each circle indicates a site. A solid (open) circle indicates a doublon (holon). Thin arrows denote virtual hopping processes in the strong-coupling expansion. (a) Configuration with no doublon; a basis for $U/t \to \infty$. (b) A doublon sits at a nearest neighbor of a holon; a virtual state in the second order of strong-coupling expansion in t/U. (c) A doublon sits at a diagonal neighbor of a holon; a virtual state in the second (fourth) order in t'/U (t/U). (d) A doublon sits at a farther site from a holon; a higher-order virtual state. For the case of eq. (4), we set $\mu' = 0$.

$$\frac{\langle \Psi_G | \mathcal{H}_{t-J} | \Psi_G \rangle}{\langle \Psi_G | \Psi_G \rangle} \sim \frac{\langle \Psi_G e^{iS} | \mathcal{H}_{\text{Hub}} | e^{-iS} \Psi_G \rangle}{\langle \Psi_G e^{iS} | e^{-iS} \Psi_G \rangle}. \tag{6}$$

Thus, an improved wave function for the Hubbard model is given by applying the strong-coupling expansion, e^{-iS}, to a Gutzwiller-type function Ψ_G ($= \mathcal{P}_G \Phi$). Considering virtual hopping processes in this expansion, as shown in Fig. 2, one easily notices that the first-order terms of this expansion roughly correspond to $\mathcal{P}_Q \Psi_G$. In addition, it was found that a more direct form of $e^{-iS} \Psi_G$ yields improved results[36] similar to those of $\mathcal{P}_Q \Psi_G$, mentioned in the following sections.

In the early VMC study of the projected Fermi sea, $\Psi_Q^{\text{FS}} = \mathcal{P}_Q \mathcal{P}_G \Phi_F$, for the 1D and 2D square lattices, Yokoyama and Shiba[27] concluded that Ψ_Q^{FS} corrects the shortcomings (1) and (2), mentioned above, of the GWF, but a Mott transition does not arise, even in Ψ_Q^{FS}. Subsequently, Millis and Coppersmith[37] also concluded, by calculating the zero-frequency part of the optical conductivity using a VMC technique, that a Mott transition cannot be described in terms of this type of wave function. However, as we have repeatedly explained in previous papers,[6,38] these early studies were not sufficiently thorough or careful to arrive at the correct conclusion that the doublon–holon binding factor $\mathcal{P}_Q$ is essential for describing a Mott transition. Actually, the existence of Mott transitions has been confirmed using $\mathcal{P}_Q$ for various systems,[39] such as the square lattice,[8,38] the anisotropic triangular lattice,[6] the kagomé lattice,[40] the checker-board lattice,[41] and a degenerate Hubbard model on the square lattice.[42]

2.3   Wave functions and VMC conditions

In this paper, we continue to study the Mott transition induced by $\mathcal{P}_Q$. Considering the lattice structure shown in Fig. 1(a), we introduce into $\mathcal{P}_Q$ the effect of doublon–holon binding between diagonal-neighbor sites μ' [$\mathbf{r} = (\pm x, \pm y)$], in addition to that of the nearest neighbors, μ [$\mathbf{r} = (\pm x, 0)$ and $(0, \pm y)$]:

$$\mathcal{P}_Q = \prod_i \left(1 - \mu Q_i^\tau\right)\left(1 - \mu' Q_i^{\tau'}\right), \tag{7}$$

$$Q_i^{\tau(\tau')} = \prod_{\tau(\tau')} [d_i(1 - e_{i+\tau(\tau')}) + e_i(1 - d_{i+\tau(\tau')})], \tag{8}$$

in which τ (τ') varies over all the adjacent sites in the bond directions of t (t'). The weight assignment of the correlation

factors $\mathcal{P} = \mathcal{P}_Q \mathcal{P}_G$ is explained in Fig. 2. For the pure square lattice ($t' = 0$), we use eq. (4) instead of eq. (7) for simplicity, because we can confirm that the effect of μ' is negligible, even quantitatively, for $t' = 0$. The wave function we deal with in this paper is

$$\Psi_Q = \mathcal{P}_Q \mathcal{P}_G \Phi. \tag{9}$$

As a one-body part Φ, we primarily study a fixed-density BCS state:[43]

$$\Phi_d = \left(\sum_{\mathbf{k}} a_{\mathbf{k}} c_{\mathbf{k}\uparrow}^\dagger c_{-\mathbf{k}\downarrow}^\dagger\right)^{N_e/2} |0\rangle, \tag{10}$$

$$a_{\mathbf{k}} = \frac{v_{\mathbf{k}}}{u_{\mathbf{k}}} = \frac{\Delta_{\mathbf{k}}}{\varepsilon_{\mathbf{k}} - \zeta + \sqrt{(\varepsilon_{\mathbf{k}} - \zeta)^2 + \Delta_{\mathbf{k}}^2}}, \tag{11}$$

where ζ is a variational parameter that is reduced to the chemical potential for $U/t \to 0$. Since we know that, at half filling, the simple $d_{x^2-y^2}$ wave is the most stable among the various gap shapes,[32,33,44] here we exclusively consider the d-wave gap:

$$\Delta_{\mathbf{k}} = \Delta_d(\cos k_x - \cos k_y). \tag{12}$$

Note that although the variational parameter Δ_d indicates the magnitude of the d-wave gap, a state ($\Psi_Q^d = \mathcal{P}\Phi_d$) with finite Δ_d does not necessarily mean a SC state.[45] We fix the value of t' in $\varepsilon_{\mathbf{k}}$ in the wave function [eq. (11)] at the same value as that in the Hamiltonian, because the renormalization of $\varepsilon_{\mathbf{k}}$[46] is not significant when the system is conductive,[6] and ζ compensates this effect to some extent in the insulating regime, as we will see later. For $\Delta_d = 0$, Φ_d is reduced to Φ_F, which is explained next.

As a reference state, we also study the Fermi sea,

$$\Phi_F = \prod_{k < k_F, \sigma} c_{\mathbf{k}\sigma}^\dagger |0\rangle. \tag{13}$$

A complication is that Ψ_Q^{FS} ($= \mathcal{P}_Q \mathcal{P}_G \Phi_{\text{FS}}$) does not merely represent a normal state; Ψ_Q^{FS} also undergoes a Mott transition, as we found for the attractive Hubbard model.[38] The results of the attractive model for the symmetric case ($t' = 0$ and $n = 1$) can be exactly mapped to those of the repulsive model through a canonical transformation.[47] As an extension in this paper, we study the properties of Ψ_Q^{FS} for asymmetric cases ($t' \neq 0$).

For the comparison made in §5 and §6, we consider an ordinary mean-field solution Φ_{AF}[48] for a one-body AF state with a long-range order. In the trial AF state,

$$\Psi_Q^{\text{AF}} = \mathcal{P}_Q \mathcal{P}_G \Phi_{\text{AF}}, \tag{14}$$

the AF gap Δ_{AF} is optimized as a parameter, but t' in $\varepsilon_{\mathbf{k}}$ is fixed at the model value, similarly to that in Ψ_Q^d.

Because our trial functions have at most five parameters to be optimized [g, μ, μ', $\Delta_{d(\text{AF})}$, ζ], we have used a simple version of optimization VMC methods,[49] namely a line minimization of one parameter with the others fixed.[50] In one round of iteration, every parameter is optimized once. In most cases of optimization in this study, the parameters converge within 2 or 3 rounds, after which we continue the optimization process for another 15–20 rounds. The optimized values of the parameters and energy are determined by averaging the results of these rounds after convergence. Because each optimization procedure is

carried out with typically 2.5×10^5 ($L = 10$–14) samples, preserving the acceptance ratio of 0.5, our data are practically the averages of 3–5 million samples. Thereby, the accuracy in the total energy is markedly increased, typically to the order of $10^{-4}t$. Because the convergence of optimization becomes very slow near phase transitions, particularly continuous transitions, we carried out longer iterations (~ 50 rounds) in such cases. With the optimized parameters thus determined, physical quantities are calculated in different VMC simulations with 2.5×10^5 samples. We used lattices of $L \times L$ sites ($L = 6$–18, mainly 10–14) with periodic-antiperiodic boundary conditions. Because the closed-shell condition cannot be satisfied in a wide range of asymmetric model parameters ($t' \neq 0$) at half filling, we are often obliged to calculate with open shells.

Finally, we mention finite-size analysis in this study. In the symmetric case ($t' = 0$), the system-size dependence of various quantities is often monotonic, because the **k**-point structure included in the Fermi surface becomes systematic with increasing L. In contrast, in asymmetric cases, the **k**-point structure is unique to each system size L and frustration strength t'; therefore, the system-size dependence becomes irregular, and the t'/t dependence is not smooth.

3. Mott Transitions in *d*-Wave State

In this section, we study Mott transitions arising in the *d*-wave singlet state Ψ_Q^d. In §3.1, we show that a first-order transition occurs by observing hysteresis in the U/t dependence of total energy. In §3.2, we identify this critical behavior as a Mott transition without relevance to magnetic orders by studying various quantities. In §3.3, we consider the properties of this transition with reference to other studies.

3.1 Total energy and hysteresis behavior

First, let us consider the behavior of the optimized total energy per site, E. In the inset of Fig. 3, E/t for $t'/t = 0$ is plotted for a wide range of U/t and four system sizes (L). On this scale, L dependence is imperceptible. One readily notices a cusp at $U/t \sim 6.5$, where the data points of various L are concentrated. In the main panel of Fig. 3, this cusp is magnified. We have optimized the wave function successively, from both weak- and strong-correlation sides toward this cusp. For the system with $L = 10$, the optimized energies from the two sides coincide, and E/t becomes a smooth function of U/t. On the other hand, for larger systems ($L \geq 12$ in Fig. 3), the optimized values in the weak-correlation side are not smoothly connected to those in the strong-correlation side, and *vice versa*.[51] At the cusp, all optimized variational parameters have discontinuities, as shown in Figs. 4(a)–4(e). Such hysteresis and discontinuities indicate that a first-order phase transition occurs at the cusp point ($U = U_c$). In the following subsection, we identify this transition as a Mott (conductor-to-nonmagnetic-insulator) transition.

Next, we study the L dependence of the critical point. We first note that it is essential to check the system-size dependence when we consider critical phenomena, as we have learned from the distinct behavior between $L = 10$ and $L \geq 12$ in Fig. 3. As the system size increases ($L \geq 12$), the critical point shifts to a larger value of U/t (Fig. 3). This is
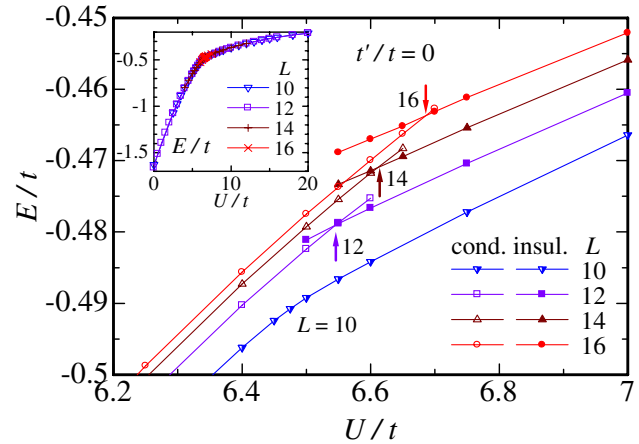

Fig. 3. (Color online) Total energies of *d*-wave state for pure square lattice ($t' = 0$) for four system sizes near critical points (U_c), indicated by arrows. Hysteresis is observed for $L = 12$–16; the local minima for the conductive (insulating) sides are denoted by open (solid) symbols. For $L = 10$, hysteresis is not observed using the present VMC calculations, and the parameters vary continuously. The critical values are $U_c/t = 6.54$, 6.61, and 6.69 for $L = 12$, 14, and 16, respectively. Inset: The behavior of E/t over a wider range of U/t.

partly because a large system size is more advantageous to conductive states, which have longer correlation lengths. For $t'/t = 0$, because the system-size dependence of E/t is fitted well with quadratic curves of $1/N_s$, the critical value for $L = \infty$ can be estimated as $U_c/t = 7.0 \pm 0.1$ using the method of least squares.

Here, we consider the t'/t dependence. As shown in Fig. 4(f), the total energy E/t also has a cusp for finite t'/t. The behavior of E/t near the cusps is magnified in Fig. 5 for four values of t'/t and for $L = 12$. For $U < U_c$, E/t is significantly reduced as $|t'/t|$ increases; this behavior is common to the noninteracting case, in which the gain in $E_{t'}$ exceeds the loss in E_t [E_t ($E_{t'}$): the contribution from the t (t') term to $\langle \mathcal{H}_{\mathrm{kin}} \rangle$]. In contrast, for $U > U_c$, E/t changes only very slightly; we will return to this point in §3.3. Consequently, as $|t'/t|$ increases, the transition point shifts to a larger value of U/t, particularly rapidly for large t'/t, although the bandwidth remains constant, $8t$, for $0 \leq t'/t \leq 0.5$. This t'/t dependence of U_c/t can be verified from the behavior of the parameters [Figs. 4(a)–4(e)].

In Fig. 6, we show the system-size dependence of E/t near U_c/t for strongly frustrated cases ($t'/t = -0.4$ and -0.5). Here, even the system as small as $L = 10$ exhibits clear hysteresis. The critical value U_c/t tends to increases monotonically as L increases, although the extrapolation of U_c/t to $L = \infty$ is difficult using the present data, because of the nonmonotonic system-size dependence, as mentioned. However, we predict that U_c/t for $L = \infty$ is only slightly larger than those for finite L, because the rate of increase of U_c/t with respect to L is similar to that for $t'/t = 0$.

3.2 Confirmation of Mott transition

In this subsection, we confirm that the above transition is a Mott transition by studying various quantities.

First, we consider the doublon–holon binding factor μ, which is a good indicator of the Mott transition. In Fig. 4(c),
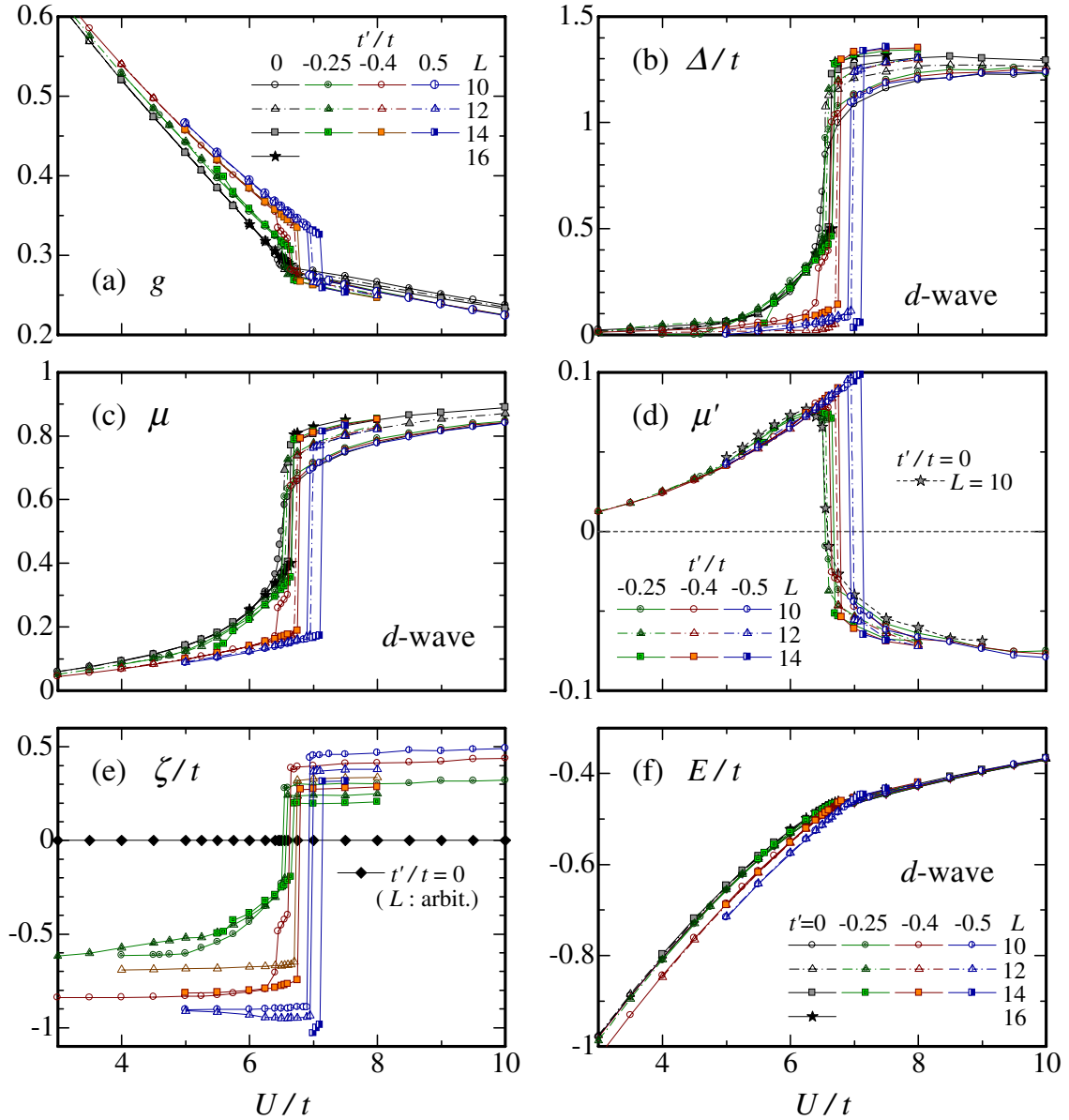
Fig. 4. (Color online) (a)–(e) Optimized variational parameters (at the global minima of E/t) for d-wave state near critical values U_c as function of U/t: (a) Onsite correlation (Gutzwiller) factor. (b) d-wave gap parameter. (c) Doublon–holon binding factor between nearest-neighbor sites. (d) The same factor between diagonal-neighbor sites. (e) Chemical potential. For $t' = 0$, ζ is always zero owing to the band symmetry. (f) Total energies for four values of t'/t. The symbols and abscissa scales are common to all the panels. Data for four values of t'/t, and for three or four system sizes ($L \times L$) are compared.

the optimized value of μ is plotted as a function of U/t. For each t'/t and L, except for $t' = 0$ and $L = 10$, μ has a discontinuity and suddenly increases at $U = U_c$. Note that for $U < U_c$, μ primarily depends on t'/t and slightly on L in relation to SC, as mentioned later, whereas for $U > U_c$, μ significantly increases as L increases, but is almost independent of t'/t. Thus, in the strong-correlation side $U > U_c$, μ has a value close to 1,[52] which means that almost all doublons and holons are bound within nearest-neighbor sites. This situation is shown in the snapshots taken in the VMC sampling process (Fig. 7). On the weak-correlation side of U_c [Fig. 7(a)], where μ has a relatively small value, doublons (negative charge carriers) are often isolated from holons (positive charge carriers). Thus, charge can move substantially, and the system is considered conductive. On the other hand, for $U > U_c$ [Fig. 7(b)], each doublon is, in

most cases, paired with a holon, in addition to there being a decrease in the carrier number. It follows that free charged particles rarely exist.

Second, we consider the doublon density,

$$d = \frac{1}{N_s} \sum_i n_{i\uparrow} n_{i\downarrow} = \frac{E_U}{U}, \tag{15}$$

which is regarded as the order parameter of Mott transitions,[28,53,54] by analogy with the particle density in gas–liquid transitions. In eq. (15), $E_U = \langle \mathcal{H}_{\text{int}} \rangle / N_s$. In the inset of Fig. 8, d is plotted for four values of t'/t and for various system sizes. As U/t increases, d decreases linearly from the noninteracting value 0.25, but at $U = U_c$, it suddenly drops to a considerably smaller value, and then decreases slowly for $U > U_c$. In the main panel of Fig. 8, the vicinity of the critical point is magnified; the discontinuity of d at U_c is
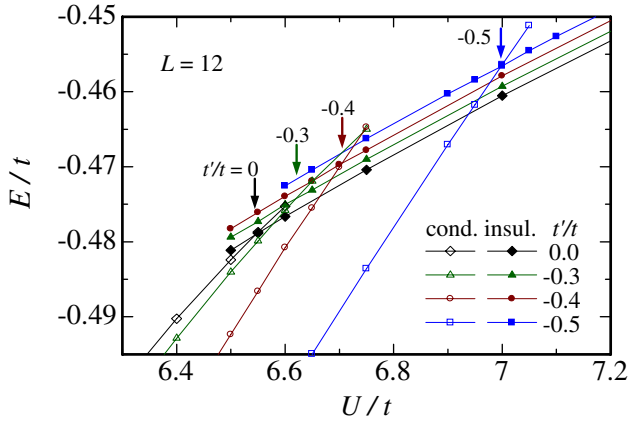
Fig. 5. (Color online) Total energies for four values of t'/t near critical points indicated by arrows. The system size is fixed at $L = 12$. Hysteresis is observed for each case. The local minima for the conductive (insulating) sides are shown by open (solid) symbols. The critical values are $U_c/t = 6.54$, 6.62, 6.70, and 7.00 for $t'/t = 0$, -0.3, -0.4, and -0.5, respectively.
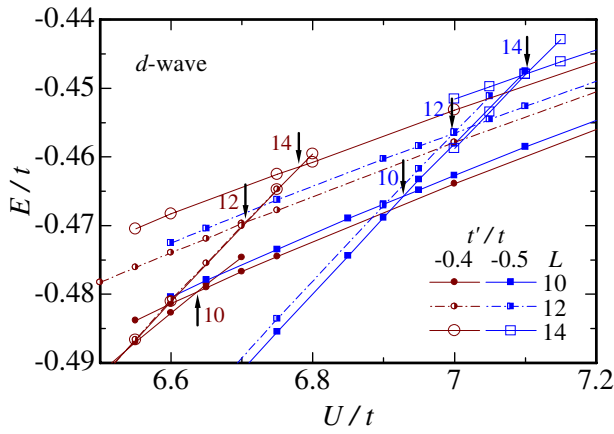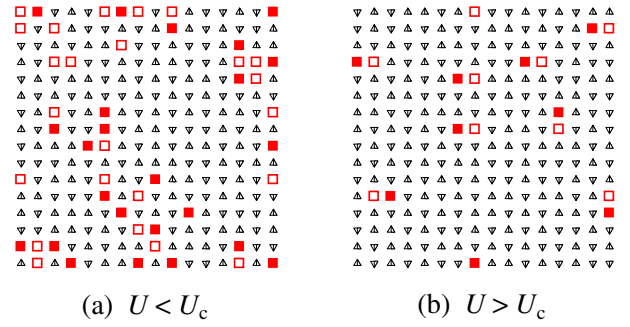

Fig. 7. (Color online) Snapshots (typical electron configurations) taken in VMC sampling process of d-wave state for $t'/t = 0$ and $L = 16$ ($U_c/t = 6.69$). (a) $U/t = 6.25$ ($\mu = 0.30$), slightly less than U_c, and (b) $U/t = 7.50$ ($\mu = 0.85$), slightly greater than U_c. Closed and open squares, upward and downward triangles denote doublons, holons, ↑- and ↓-spins, respectively.

Fig. 6. (Color online) Total energies for strongly frustrated cases ($t'/t = -0.4$ and -0.5) near critical points, indicated by arrows, for three system sizes. Hysteresis is observed for every case; the conductive and insulating cases are denoted by the same symbols. The critical values are $U_c/t = 6.64$, 6.70, and 6.78 for $L = 10$, 12, and 14, respectively, for $t'/t = -0.4$, and similarly, $U_c/t = 6.93$, 7.00, and 7.10 for $t'/t = -0.5$.
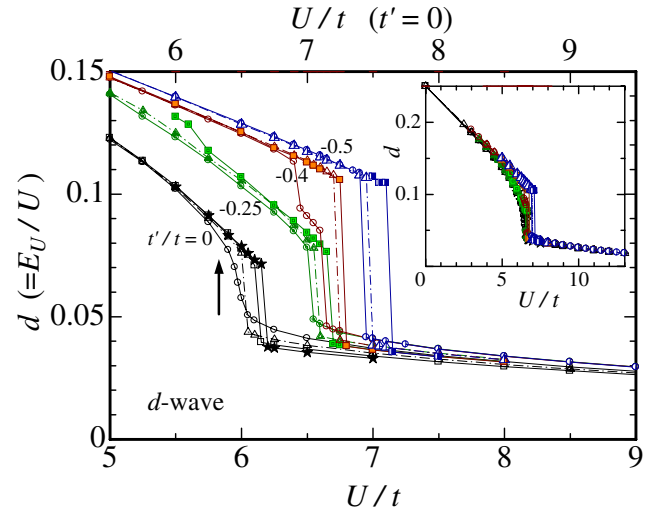

Fig. 8. (Color online) Density of doublons (doubly occupied sites) obtained with Ψ_d as a function of U/t for four values of t'/t. For each t'/t, various system sizes ($L = 10$–16) are simultaneously plotted. The symbols are common to Fig. 4. For $t'/t = 0$, the horizontal axis is shifted by 0.5 (see upper axis) for clarity. In the inset, the same curves are shown over a wider range.

clear for each case. This abrupt decrease in doublon density can actually be verified in Fig. 7, where the number of doublons is 24 ($d = 0.094$) for $U/t = 6.25$, and 9 ($d = 0.035$) for $U/t = 7.5$, which is consistent with the values in Fig. 8. Thus, the discontinuity of the doublon density at U_c is similar to that of the change in particle density in gas–liquid transitions.

Third, the behavior of the momentum distribution function,

$$n(\mathbf{k}) = \frac{1}{2N_s} \sum_{k,\sigma} \langle c^\dagger_{\mathbf{k}\sigma} c_{\mathbf{k}\sigma} \rangle, \qquad (16)$$

at the Fermi surface is another good indicator of a Mott transition. In Fig. 9, we show the U/t dependence of $n(\mathbf{k})$ measured with the optimized parameters along the path $\Gamma(0,0)$–X$(\pi,0)$–M(π,π)–Γ in the Brillouin zone for $t'/t = 0$. Because the present trial state is a projected d-wave, there is a node in the gap function in the Γ–M

direction, and $n(\mathbf{k})$ has a discontinuity at the Fermi surface, $\mathbf{k}_F$, in this direction if the system is metallic or SC. As shown in Fig. 9, the discontinuity at $\mathbf{k}_F$ is clear for $U < U_c$, whereas, at $U = U_c$, the behavior of $n(\mathbf{k})$ abruptly changes, and becomes a smooth function for $U > U_c$ also in the Γ–M direction; that is, the Fermi surface disappears. Thus, metallic properties are abruptly lost at $U = U_c$, even in the nodal direction of the $d_{x^2-y^2}$ wave.

To consider this behavior quantitatively, we employ the quasi-particle renormalization factor Z, which roughly corresponds to the inverse of effective mass, unless the $\mathbf{k}$-dependent renormalization of self energy is severe. We estimated Z from the magnitude of the jump in $n(\mathbf{k})$ at $\mathbf{k} = \mathbf{k}_F$ in the nodal direction, and plotted it in Fig. 10 for four values of t'/t.[55] For all the values of t'/t, Z decreases slowly for $U < U_c$, whereas at $U = U_c$, Z suddenly vanishes with a sizable discontinuity, reflecting the first-order character of the transition. The system-size dependence of Z is very small, except for minor differences near U_c. The behavior of
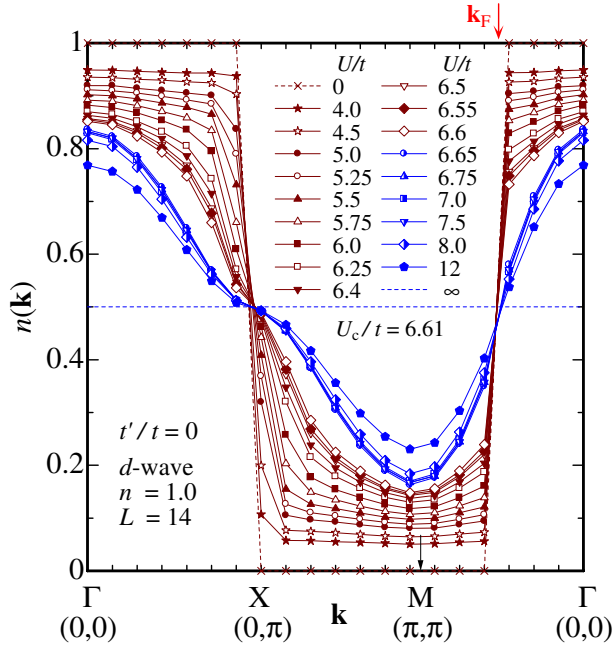
Fig. 9. (Color online) Momentum distribution function of the *d*-wave state for various values of U/t for $t'/t = 0$. The half-closed symbols and star denote the data for $U > U_c$. The arrow on the upper axis indicates the position of the Fermi surface in the node-of-gap (Γ–M) direction.
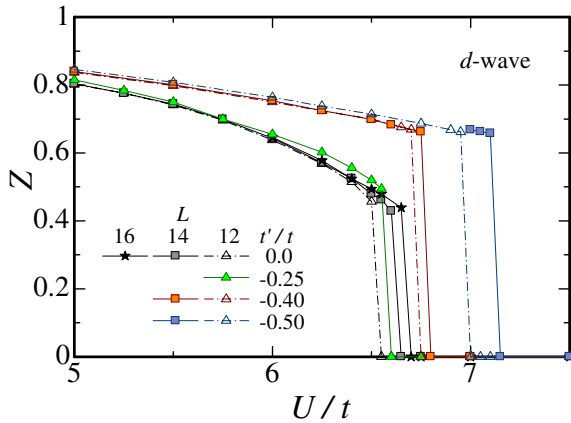

Fig. 10. (Color online) Quasi-particle renormalization factor Z of *d*-wave singlet states, estimated from discontinuities of $n(\mathbf{k})$ in node-of-gap direction. Data for four values of t'/t are plotted as a function of U/t.

Z strongly suggests that the effective electron mass diverges for $U > U_c$.

Finally, let us consider the charge structure factor,

$$N(\mathbf{q}) = \frac{1}{N_s} \sum_{i,j} e^{i\mathbf{q}\cdot(\mathbf{R}_i - \mathbf{R}_j)} \langle n_i n_j \rangle - n^2, \tag{17}$$

with $n_i = n_{i\uparrow} + n_{i\downarrow}$. Within variation theory, it is known that $N(\mathbf{q}) \propto |\mathbf{q}|$ for $|\mathbf{q}| \to 0$ if the state does not have a gap in the charge degree of freedom, whereas $N(\mathbf{q}) \propto \mathbf{q}^2$ if a charge gap opens. In Fig. 11, we show the U/t dependence of $N(\mathbf{q})$ for $t'/t = -0.25$ and -0.4. For $U < U_c$, the behavior of $N(\mathbf{q})$ near the Γ point seems linear in $|\mathbf{q}|$ for both values of t'/t. The behavior of $N(\mathbf{q})$ abruptly changes at the critical point, and seemingly becomes quadratic in $|\mathbf{q}|$ for $U > U_c$. Although it is not easy to definitely determine the power of
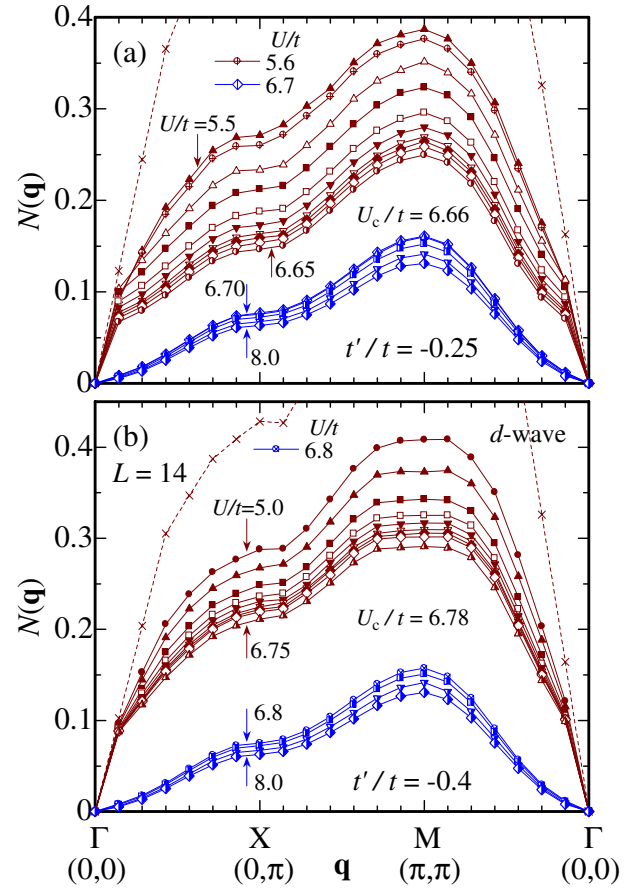

Fig. 11. (Color online) U/t dependence of charge structure factor for *d*-wave state ($L = 14$) for (a) $t'/t = -0.25$ and (b) $t'/t = -0.4$. The two panels are in the same scale. The symbols in both panels are common to Fig. 9 except for the values of U/t specified here.
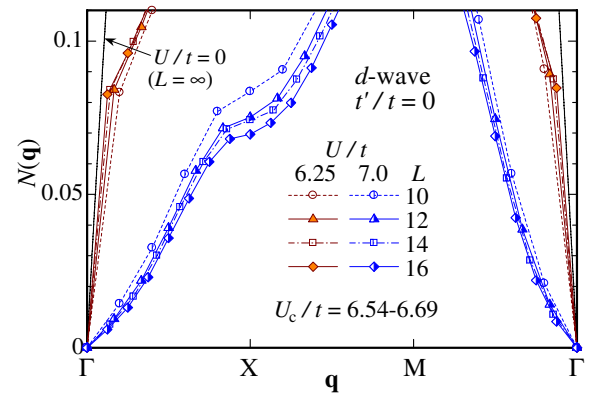

Fig. 12. (Color online) System-size dependence of charge structure factor in *d*-wave state ($t'/t = 0$) near Γ point for $U = 6.25t$ ($< U_c$) and $U = 7.0t$ ($> U_c$).

$N(\mathbf{q})$ for the small systems used here, we find that the size dependence is different for $U < U_c$ and for $U > U_c$. As shown in Fig. 12, the behavior of $N(\mathbf{q})$ near the Γ point for $U < U_c$ approaches the analytic curve of $U/t = 0$ ($L = \infty$) as L increases. Conversely, for $U > U_c$, the slope of $N(\mathbf{q})$ for $|\mathbf{q}| \to 0$ becomes smaller as L increases, suggesting the quadratic behavior of $N(\mathbf{q})$. It follows that Ψ_Q^d is gapless in the charge sector and conductive for $U < U_c$, but a charge gap probably opens for $U > U_c$ and Ψ_Q^d becomes insulating.
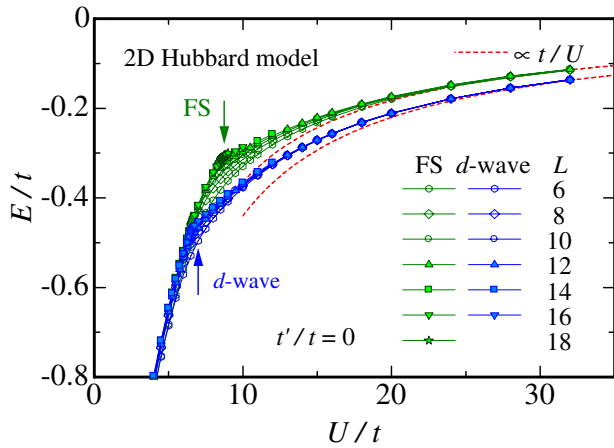
Fig. 13.   (Color online) Total energy of projected Fermi sea and *d*-wave states for $t'/t = 0$ as a function of U/t for several system sizes. The Mott critical points for both cases are indicated by arrows. Red dashed lines are fitted curves proportional to t/U. As expected from Fig. 4(f), the results for $|t'/t| > 0$ almost coincide with the present curves for $t'/t = 0$ in the insulating regime.

Fig. 14.   (Color online) U/t dependence of spin structure factor in *d*-wave state for $t'/t = 0$ and $L = 14$ ($U_c/t = 6.61$). The inset shows the magnification of the region near the Γ point on the Γ–X line, and the symbols are common to the main panel. $S(\mathbf{q})$ on the Γ–M line (nodal direction) exhibits basically the same behavior for small $|\mathbf{q}|$. Data points of different Us for $U > U_c$ almost overlap one another.

Because of the behavior of all the quantities discussed above, it is appropriate to judge that a first-order Mott transition occurs in the *d*-wave singlet state at $U = U_c$ for the arbitrary values of t'/t considered.

3.3   Properties of Mott transitions

Most of the properties of the Mott transition in Ψ_Q^d in the present model, eq. (1), are shared with those studied in the preceding report for the anisotropic triangular lattice.[6] In such cases, we avoid repeating detailed explanations, and only give a brief summary.

(1) In contrast to the behavior in Brinkman–Rice theory,[53] in which electrons cease moving and doublons completely vanish in the insulating regime, the present VMC result exhibits energy reduction broadly proportional to $-t^2/U$ ($= -J/4$) for $U > U_c$, as shown in Fig. 13. Thus, as we argued in a previous letter,[8] the results of strong-coupling theories (*t*–*J*-type models) are qualitatively useful for $U > U_c$; the value of U_c is roughly equal to the bandwidth.[33]

(2) As the frustration t'/t increases, the character of the first-order phase transition becomes notable. For example, as t'/t increases, the hysteresis in E/t is observed in smaller systems, and the magnitude of discontinuity at $U = U_c$ for the variational parameters and quantities such as d and Z increases.

(3) In the insulating regime, Ψ_Q^d tends to exhibit gaplike behavior in the spin structure factor,

$$S(\mathbf{q}) = \frac{1}{N_s} \sum_{ij} e^{i\mathbf{q}\cdot(\mathbf{R}_i - \mathbf{R}_j)} \left\langle S_i^z S_j^z \right\rangle, \qquad (18)$$

for small $|\mathbf{q}|$. As seen in the inset of Fig. 14, for $t' = 0$, $S(\mathbf{q})$ is a linear function of $|\mathbf{q}|$ at $U/t = 0$; as U/t increases, $S(\mathbf{q})$ becomes a quadratic function of $|\mathbf{q}|$, suggesting that a SC gap opens and becomes large, as will be mentioned in §5. For $U > U_c$, the quadratic behavior of $S(\mathbf{q})$ becomes clearer; it is possible that a spin gap opens in the insulating regime. As discussed later, the frustration makes no difference at this point.
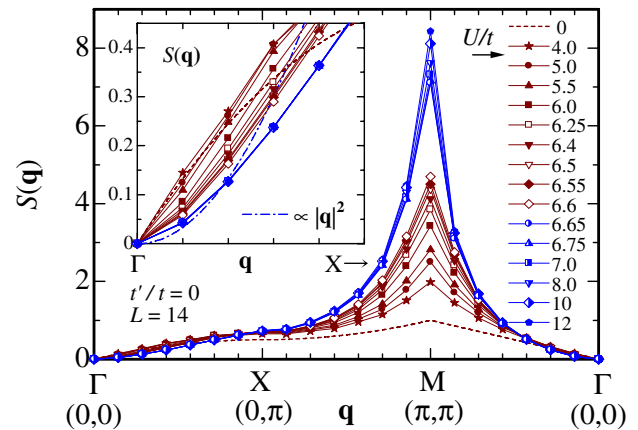
This gaplike behavior is in contrast to the case of Ψ_Q^{FS}, as will be argued in §4. Strictly, however, the insulating state represented by Ψ_Q^d can be gapless in the spin sector, in the same manner that the *d*-wave SC is gapless in the node direction. To settle this point, further studies are necessary.

(4) In the preceding study for the anisotropic triangular lattice,[6] a band renormalization effect[46] is taken into account by optimizing t' in Ψ_Q^d as a variational parameter, independently of t' given in the Hamiltonian. In the insulating regime, the effective t' is significantly reduced to an almost nonfrustrated value, namely $t'/t \sim 0$. Thereby, the Fermi surface almost recovers the nesting condition for the square lattice, leading to highly developed short-range AF correlation. In the trial states studied here, the band renormalization effect is not included, but the various results are quantitatively similar to those of the previous study, and the AF correlation considerably increases for $U > U_c$, as shown in Figs. 14 and 25. This result is mainly caused by the behavior of the chemical potential ζ [Fig. 4(e)],[56] which changes its sign for $U > U_c$ so as to recover the nesting condition, instead of by the band renormalization.

(5) In Table I, we show the optimized parameters in the insulating regime ($U > U_c$) for various t'/t. Note that the parameters vary only very slightly, except for ζ/t; the optimized Ψ_Q^d is almost unchanged with varying t'/t. In Table II, we list the total energy and energy components for $U > U_c$, calculated using the optimized Ψ_Q^d. E is again almost independent of t'/t, because $E_{t'}$ makes a very slight contribution, even for large t'/t (see also Table III). As shown in the final column of Table II, the AF spin correlation retains a considerably large value for large t'/t. This indicates that Ψ_Q^d is stabilized by preserving the nesting condition for the square lattice; in other words, the quasi-Fermi surface is retained at the gap maxima $(\pi, 0)$ and $(0, \pi)$, at the cost of the energy reduction due

Table I. Optimized variational parameters of two wave functions, Ψ_Q^d and Ψ_Q^{FS}, studied in §4, in respective insulating regimes ($U > U_c$) for various t'/t. The final digits may include some errors. $L = 14$.

Ψ	$|t'/t|$	g	Δ_d/t	μ	μ'	ζ/t
Ψ_Q^d	0.0	0.266	1.291	0.831	—	0.0
($U = 7.5t$)	0.25	0.254	1.339	0.840	-0.0677	0.200
	0.3	0.254	1.335	0.837	-0.0665	0.230
	0.4	0.254	1.349	0.837	-0.0690	0.279
	0.5	0.253	1.355	0.832	-0.0688	0.317
Ψ_Q^{FS}	0.0	0.140	—	0.923	—	—
($U = 12t$)	0.25	0.119	—	0.904	0.0776	—
	0.4	0.121	—	0.829	0.1317	—

Table II. Three energy components, total energy and spin structure factor at AF wave number, calculated using Ψ_Q^d and Ψ_Q^{FS} in respective insulating regimes ($U > U_c$) for various t'/t. $L = 14$. The final digits may include some errors. Because each energy component and E/t are averaged independently, E/t does not precisely coincide with the sum of its components.

Ψ	$|t'/t|$	E_t/t	$E_{t'}/t$	E_U/t	E/t	$S(\mathbf{G})$
Ψ_Q^d	0.0	-0.6922	0.0	0.2548	-0.4384	7.54
($U = 7.5t$)	0.25	-0.6888	-0.0008	0.2533	-0.4375	7.28
	0.3	-0.6899	-0.0012	0.2532	-0.4370	7.27
	0.4	-0.6848	-0.0019	0.2529	-0.4357	7.06
	0.5	-0.6829	-0.0033	0.2522	-0.4340	6.90
Ψ_Q^{FS}	0.0	-0.4383	0.0	0.1809	-0.2575	15.93
($U = 12t$)	0.25	-0.3455	-0.0018	0.1576	-0.1899	3.81
	0.4	-0.3276	-0.0053	0.1573	-0.1752	2.09

Table III. Comparison of ratio $\rho = E_{t'}/E_t$ among the different phases indicated in the brackets for the d-wave state and the projected Fermi sea. The abbreviations "ins." and "wSC" denote insulating and weak SC, respectively. The systems of $L = 14$ is used. Values of ρ are shown as percentages.

Ψ	$|t'/t|$	U/t			
		0	6.25	7.5	13
Ψ_Q^d	0.25	3.3	1.4 (SC)	0.12 (ins.)	—
	0.4	8.8	7.6 (wSC)	0.28 (ins.)	—
Ψ_Q^{FS}	0.25	3.3	3.3 (metal)	3.2 (metal)	0.4 (ins.)
	0.4	8.8	8.8 (metal)	8.5 (metal)	1.1 (ins.)

to the diagonal hopping or frustration. Thus, the AF correlation is a key factor for stabilizing Ψ_Q^d.

Regarding the AF correlation, it is known for the SC states with d-type symmetries that the gap maxima overlap with the hot spot, namely, the intersection of the Fermi surface and the magnetic Brillouin zone boundary.[44] Thus, it is possible that the shape of the gap function $\Delta_{\mathbf{k}}$ deviates from that of the simple d-wave, particularly for large t'/t. This is an interesting future problem.

4. Mott Transitions in Projected Fermi Sea

In this section, we discuss the Mott transition in Ψ_Q^{FS} as a continuation of the previous studies for $t'/t = 0$.[8,38] This transition has features different from those of Ψ_Q^d, although Ψ_Q^{FS} always has a higher energy than Ψ_Q^d within the present model. In §4.1, we make a careful analysis for $t' = 0$.

In §4.2, we consider the t'/t dependence, and contrast the properties in Ψ_Q^{FS} with those in Ψ_Q^d.

4.1 Case for $t' = 0$

The existence of a Mott transition in Ψ_Q^{FS} for $t'/t = 0$ was first pointed out in ref. 38, in which the critical value was estimated as $U_c/t \sim 8.8$ by analyzing the cusplike behavior in energy components and the discontinuity in $n(\mathbf{k})$ for $L = 10$ and 12. For these sizes, the transition appeared continuous. Certainly, we can find cusplike behavior in Fig. 13 [or in the main panel of Fig. 15(d)], where the U/t dependence of total energy is shown. Because the system-size dependence is considerably large near the cusp, we show the magnification in the vicinity of the cusp in the inset of Fig. 15(d). For $L \leq 14$, E/t is a smooth function of U/t and has a unique optimized value, whereas for $L = 16$ and 18, E/t exhibits hysteresis or double-minimum behavior near the critical point, $U_c/t = 8.59$ and 8.73, respectively, as in the case of Ψ_Q^d studied in the preceding section. Correspondingly, the two variational parameters, g and μ, exhibit discontinuities at U_c for $L \geq 16$, as shown in Figs. 15(a) and 15(b), although their magnitudes are small compared with those of Ψ_Q^d in Figs. 4(a) and 4(c). Thus, this transition, at least for $t'/t = 0$, is ascertained to be of the first order.

In Fig. 16, the doublon density is plotted as a function of U/t. At the critical point U_c, the order parameter d of Mott transitions has a discontinuity for $L \geq 16$, and suddenly drops to a small value. Simultaneously, the doublon–holon binding parameter μ becomes large and approaches 1, as shown in Fig. 15(b). These results again suggest that this transition is a Mott transition with the doublon–holon binding mechanism similar to that of Ψ_Q^d. Actually, we have verified that the feature of electron configurations is considerably different for $U < U_c$ and for $U > U_c$ (not shown), as in Fig. 7.

The transition is corroborated by the behavior of $n(\mathbf{k})$ and $N(\mathbf{q})$, in the same way as for the d-wave state. In Fig. 17, $n(\mathbf{k})$ [eq. (16)] is plotted along the path Γ–X–M–Γ for various values of U/t. Because Ψ_Q^{FS} is metallic for $U < U_c$, the Fermi surface can be defined in any direction; in this path, $\mathbf{k}_F$ points are located at the X point and at the midpoint of the Γ–M segment. For $U < U_c$, the discontinuities are apparent at both points of $\mathbf{k}_F$, whereas for $U > U_c$, the discontinuities vanish, indicating a gap opening. In Fig. 18, we show the magnitude of discontinuity, Z, measured at the X point, because the extrapolation error is small. As U/t increases, the quasi-particle renormalization factor, Z, monotonically decreases, and vanishes at U_c; the effective mass diverges, and Ψ_Q^{FS} becomes insulating. For $L \leq 14$, Z is continuous near U_c, as reported in Fig. 17 in ref. 38, whereas Z has an appreciable discontinuity at U_c for $L \geq 16$ and probably for $L = \infty$. Incidentally, the discontinuity in Z in Ψ_Q^{FS} is smaller than that in Ψ_Q^d (Fig. 10); the character of the first-order transition is less conspicuous in Ψ_Q^{FS}. In contrast, in dynamical mean-field theory for the hypercubic lattice,[57] Z continuously decreases and vanishes at $U = U_c$ without a discontinuity.

In Fig. 19, $N(\mathbf{q})$ [eq. (17)] is plotted for various values of U/t. The behavior for small $|\mathbf{q}|$ is basically the same as that for Ψ_Q^d [Fig. 11], namely, $N(\mathbf{q}) \propto |\mathbf{q}|$ for $U < U_c$, whereas
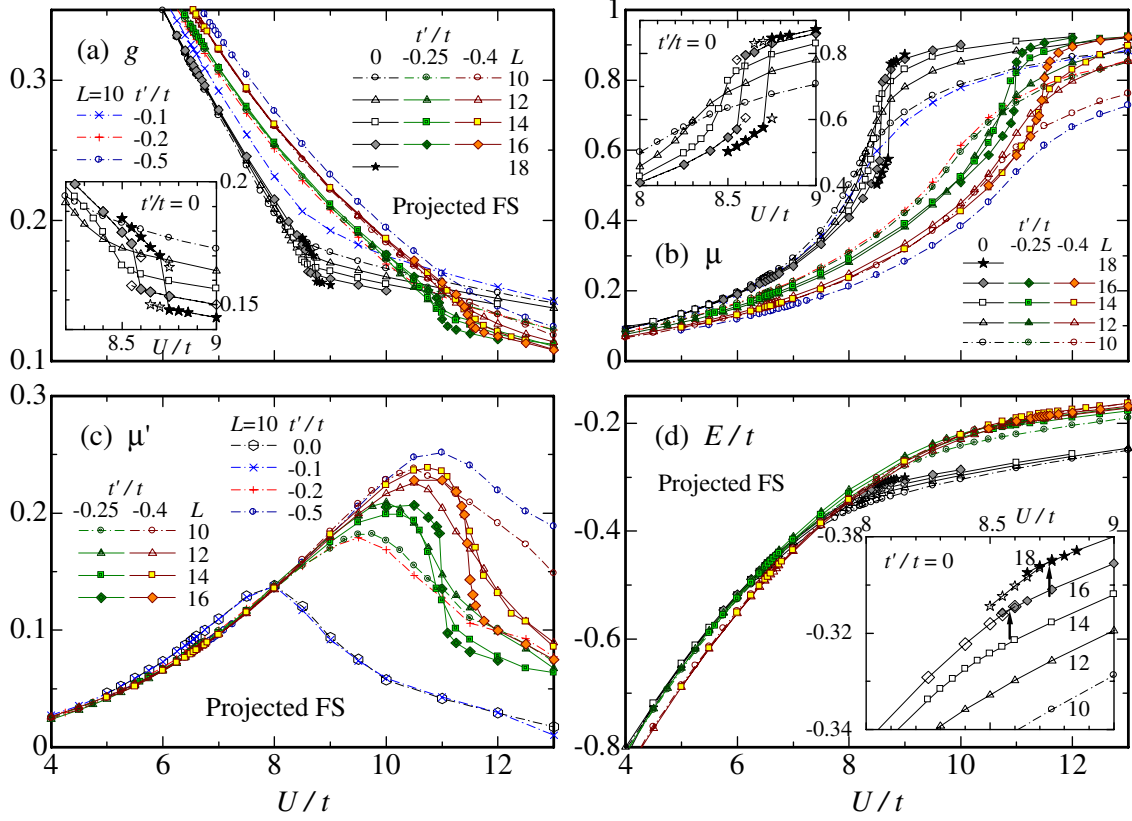
Fig. 15. (Color online) (a)–(c) Optimized variational parameters (at global minima of E/t) for projected Fermi sea Ψ_Q^{FS} as a function of U/t: (a) Onsite correlation (Gutzwiller) factor. (b) Doublon–holon binding factor between nearest-neighbor sites. The insets in (a) and (b) are magnifications near U_c for $t'/t = 0$. The data of local (but not global) minima for $L = 16$ and 18 are added using open symbols. (c) Same factor between diagonal-neighbor sites. (d) Optimized total energies for $t'/t = 0$, -0.25, and -0.4. Data for several system sizes are compared. The inset represents a magnification near U_c for $t'/t = 0$. For the data of $L = 16$ and 18, open (closed) symbols are used for the metallic (insulating) regime to emphasize the hysteresis. The critical values indicated by arrows are $U_c/t = 8.59$ and 8.73 for $L = 16$ and 18, respectively. The other symbols and the abscissa scales are common to all the main panels. In (c), we add the data of Ψ_Q^{FS} including μ' for $t'/t = 0$. Although μ' has a finite value in the metallic region, its effect is almost negligible.
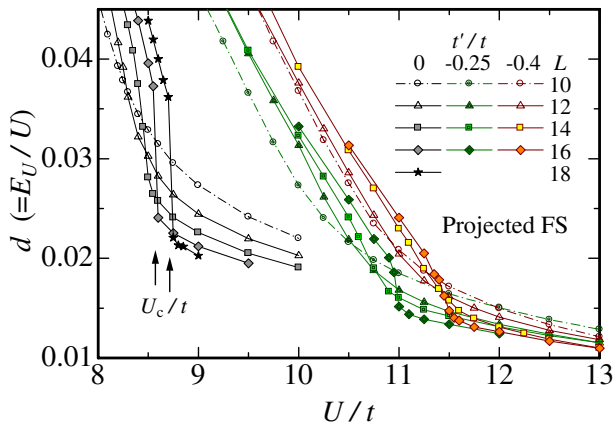

Fig. 16. (Color online) Behavior of doublon density d near the Mott critical points in the projected Fermi sea Ψ_Q^{FS} for three values of t'/t. Data of several system sizes are plotted for each t'/t. For $t'/t = 0$ and $L = 16$ and 18, the critical values of first-order transitions are indicated by arrows.

$N(\mathbf{q})$ tends to be proportional to $\mathbf{q}^2$ for $U > U_c$. This follows that a charge gap opens for $U > U_c$.

From all the above results, we regard this transition as a Mott (metal-to-nonmagnetic-insulator) transition, which is caused by the doublon–holon binding mechanism, basically

in the same way as in Ψ_Q^d.

Finally, we consider the spin degree of freedom. In Fig. 20, $S(\mathbf{q})$ [eq. (18)] is plotted for various values of U/t. As U/t increases, the AF correlation $S(\mathbf{G})$ increases, and increases abruptly near the critical point. Although the behavior of $S(\mathbf{q})$ is, as a whole, similar to that of Ψ_Q^d (Fig. 14), $S(\mathbf{G})$ is twice as large for Ψ_Q^{FS}. However, the sublattice magnetization,

$$m = \frac{1}{N_s}\left|\sum_i e^{i\mathbf{G}\cdot\mathbf{r}_i}\langle S_i^z\rangle\right|, \qquad (19)$$

remains zero within the statistical fluctuation. Thus, a long-range order is not realized, although the AF correlation is considerably enhanced in the insulating regime. Note that the behavior of $S(\mathbf{q})$ for $|\mathbf{q}| \to 0$ is linear in $|\mathbf{q}|$ for arbitrary U/t, as shown in the insets of Fig. 20, in contrast to the case of Ψ_Q^d (inset of Fig. 14). This strongly suggests that the spin gap is absent. Thus, Ψ_Q^{FS} for $U > U_c$ represents a nonmagnetic insulator without a spin gap, which is considered to be realized in κ-(ET)$_2$Cu$_2$(CN)$_3$.[58]

4.2 Effect of frustration

First, we consider the effect of frustration on the properties of the transition. In Figs. 15(a)–15(c), we show the optimized variational parameters for $t'/t = -0.25$ and -0.4, as well as $t' = 0$, for systems up to $L = 16$. Let us consider
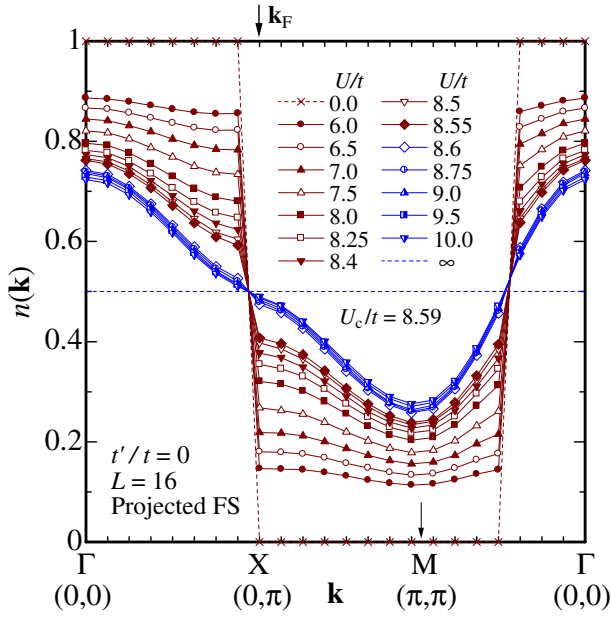
Fig. 17. (Color online) U/t dependence of momentum distribution function of Ψ_Q^{FS} for $t'/t = 0$. In this case, Z (Fig. 18) is measured at $\mathbf{k}_F$ indicated by an arrow on the upper axis (X point).
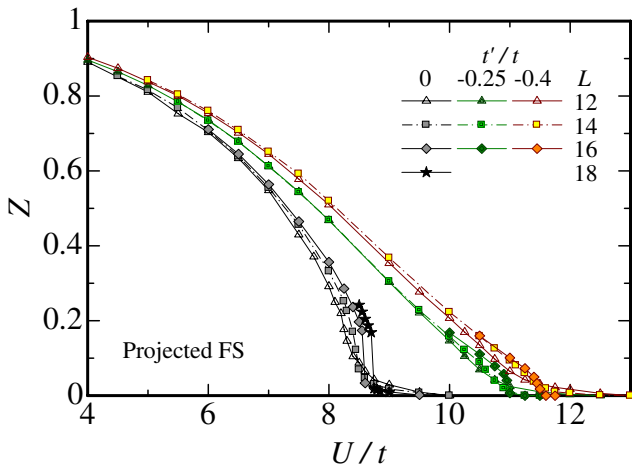

Fig. 18. (Color online) Quasi-particle renormalization factor Z of projected Fermi sea, estimated from discontinuities of $n(\mathbf{k})$ on X–M line in Brillouin zone. Data for three values of t'/t and various system sizes are plotted as a function of U/t. The tails for $U > U_c$ are mainly caused by finite-sized effects.

Fig. 19. (Color online) U/t dependence of charge density structure factor of Ψ_Q^{FS} for $t'/t = 0$. The symbols denote the same values of U/t as in Fig. 20. $U_c/t = 8.59$.

Fig. 20. (Color online) U/t dependence of spin structure factor of projected Fermi sea for $t'/t = 0$. $U_c/t = 8.59$. The insets are the close-ups near the Γ point on (a) the Γ–M line and (b) the Γ–X line.

the doublon–holon binding parameter μ [Fig. 15(b)] as a typical parameter. For small systems (e.g., $L = 10$), μ is a smoother "S"-shaped function of U/t than that for $t' = 0$. As the system size increases, μ abruptly exhibits semicritical behavior at a slightly larger U/t than that for $t' = 0$ [$U_c/t \sim 10.95$ (11.45) for $t'/t = -0.25$ (-0.4) for $L = 16$]. In contrast to the case of $t' = 0$, the cases of $t'/t = -0.25$ and -0.4 do not indicate a first-order-transition-like discontinuity or hysteresis, even for $L = 16$. In comparing the results among the three values of t'/t, we notice that the critical behavior tends to be more continuous as the frustration becomes strong. We do not consider larger systems in this work, because the statistical fluctuation around the critical points increases rapidly as L increases.
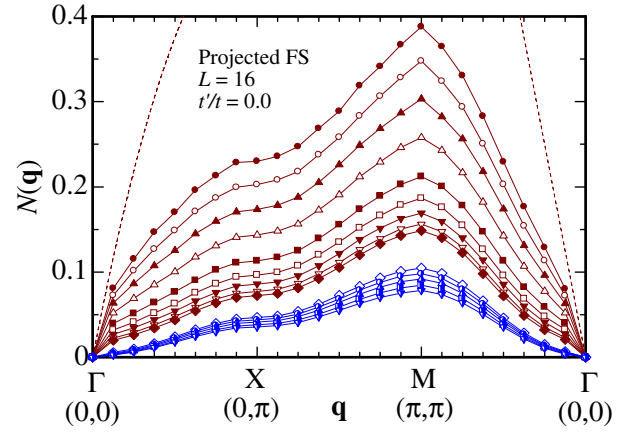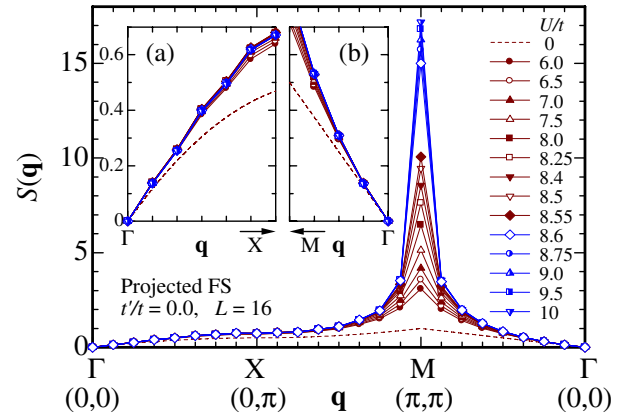
However, we assume that this size-dependent critical behavior is a sign of a first-order transition.

These features can be seen in the other variational parameters [Figs. 15(a) and 15(c)], total energy [Fig. 15(d)] doublon density (Fig. 16) and quasi-particle renormalization factor (Fig. 18). The feature that the critical properties tend to become continuous as t'/t increases is opposite to that of Ψ_Q^d studied in §3, but similar to that of the path-integral-renormalization-group approach.[17]

Next, we consider the effect of frustration on the insulating state. As shown in Table I, when t'/t varies, the optimized parameters, namely, the wave function, appreciably changes, in contrast to that of Ψ_Q^d. Accordingly, the physical quantities with respect to Ψ_Q^{FS} vary with t'/t, as shown in Table II. For energy, a notable point is that the contribution of $E_{t'}$ is still strongly suppressed in Ψ_Q^{FS}, similarly to that for Ψ_Q^d. To consider quantitatively how $E_{t'}$ behaves when U/t varies, we list the ratio $\rho \equiv E_{t'}/E_t$ in the different phases in Table III. ρ almost maintains its value of the noninteracting case ($U = 0$) in the metallic phase, but in the insulating phase, ρ drops to a very small value, although not as small as in Ψ_Q^d. This feature is affected by μ'. As seen in Fig. 15(c), μ' abruptly decreases at U_c, indicating that the doublon–holon binding in the diagonal direction, which
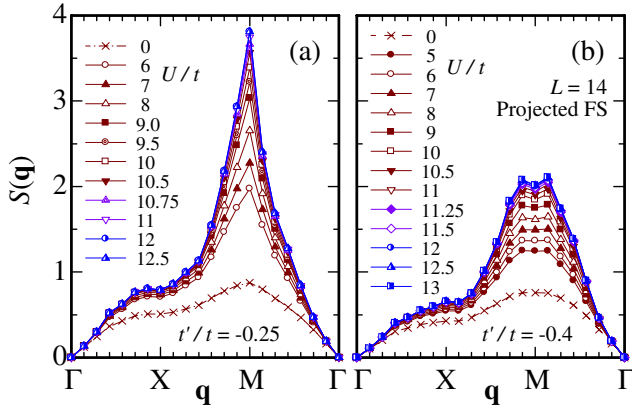
Fig. 21.   (Color online) U/t dependence of the spin structure factor of the projected Fermi sea for (a) $t'/t = -0.25$ and (b) $t'/t = -0.4$. The scale of the vertical axis is common to both panels.

assists local diagonal hopping for large U/t, also becomes less advantageous for $U > U_c$ in Ψ_Q^{FS}. The decrease in μ' is anticipated to enhance AF correlation, mentioned below.

Returning to Table II, we find that the AF spin correlation $S(\mathbf{G})$ markedly increases for $t'/t = 0$, but abruptly decreases as $|t'/t|$ increases, in sharp contrast with that of Ψ_Q^d. To elucidate the situation, we plot $S(\mathbf{q})$ for $t'/t = -0.25$ and -0.4 in Figs. 21(a) and 21(b), respectively (cf. also Fig. 20 for $t' = 0$). Although the magnitude of $S(\mathbf{G})$ abruptly decreases as $|t'/t|$ increases from 0 to 0.25, the peak position of $S(\mathbf{q})$ remains at $\mathbf{q} = \mathbf{G}$. For $t'/t = -0.4$, however, in addition to the successive decrease in magnitude, the peak of $S(\mathbf{q})$ moves to incommensurate wave numbers near the M point.

Thus, the effect of frustration is explicitly reflected in physical quantities estimated in the insulating state of Ψ_Q^{FS}.

5. $d_{x^2-y^2}$-Wave Superconductivity

In this section, we study the properties of SC arising in the d-wave singlet state Ψ_Q^d. In §5.1, we deduce the area where SC appears in the $t'-U$ plane by distinguishing, in the condensation energy, between the contributions from a SC gap and from an insulating gap. In §5.2, we confirm the appearance of SC by directly observing the d-wave pairing correlation function. In §5.3, we consider the origin of this SC.

5.1 Condensation energy

First, to determine the stability of the d-wave singlet state Ψ_Q^d, we consider its condensation energy given by

$$\Delta E = E(\Psi_Q^d) - E(\Psi_Q^F), \qquad (20)$$

where $E(\Psi)$ denotes the optimized variational energy per site with respect to Ψ. In Fig. 22(a), $\Delta E/t$ for various t'/t is plotted as a function of U/t; in Fig. 22(b), the region near the Mott critical points (U_c/t) is magnified.

Because the behavior of ΔE depends on the value of t'/t, we first consider the weakly frustrated cases ($t'/t \lesssim 0.3$). As pointed out in ref. 8, for small values of U/t ($\lesssim 5$), $\Delta E/t$ is extremely small; at intermediate values of U ($= U_{onset} \sim$ 5t–6t), $\Delta E/t$ starts to increase slowly at first, then abruptly at the Mott critical value U_c of Ψ_Q^d, where, in some cases, we can observe a mild cusp in Fig. 22(b). As U/t increases
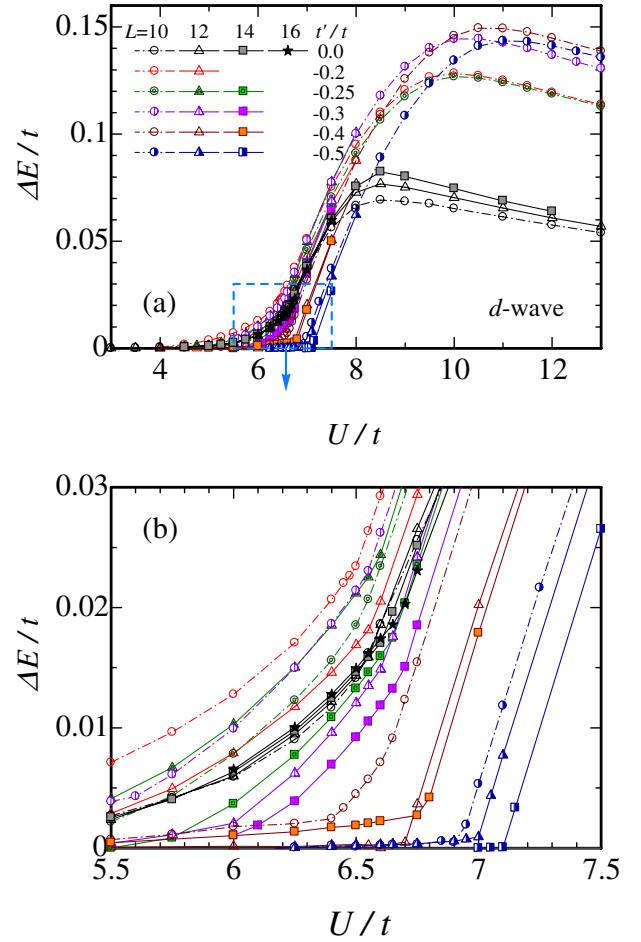

Fig. 22.   (Color online) Condensation energy, $\Delta E/t$, of d-wave singlet state as function of U/t for various values of t'/t and L. (a) $\Delta E/t$ over a wide range of U/t. (b) A close-up of $\Delta E/t$ near the Mott critical points; the range is indicated by a dashed-line box in (a). The symbols are common to (a) and (b).

further, $\Delta E/t$ has a maximum and then slowly decreases. We are now aware (§3) that, for $U > U_c$, Ψ_Q^d becomes an insulating state. Hence, the marked increase in ΔE in this regime is considered to originate from the insulating d-wave gap.[45] Consequently, the region where substantial energy reduction occurs owing to a SC gap is restricted to $U_{onset} \lesssim U < U_c$. This idea is supported by the behavior of the d-wave gap parameter Δ/t, which exhibits an appreciable increase for the corresponding values of U/t and t'/t, as shown in Fig. 4(b). Incidentally, the doublon–holon binding parameter μ increases very similarly to Δ/t [Fig. 4(c)], suggesting that this binding plays an active role in the d-wave pairing in the nearest-neighbor sites.

Next, we proceed to the strongly frustrated cases ($t'/t \gtrsim 0.4$). A major feature of ΔE, different from that in the weakly frustrated case, is that there is no substantial increase for $U_{onset} \lesssim U < U_c$. As seen in Fig. 22(b), we cannot determine U_{onset} for $t'/t = -0.4$ and -0.5, except for a special case, $t'/t = -0.4$ and $L = 10$.[59] Correspondingly, the increase in the d-wave gap Δ/t [Fig. 4(b)] is firmly suppressed in the conductive region ($U < U_c$), compared with those in the weakly frustrated cases. The behavior of μ [Fig. 4(c)] again follows that of Δ/t. Thus, SC, if there is any, is expected to be weak in this regime.

Note that the value of U/t at the maximum of $\Delta E/t$ in the insulating regime approximately corresponds to the Mott critical point of Ψ_Q^{FS}, U_c^{FS}/t, considered in §4. U_c^{FS}/t also corresponds to the crossover value, at which the character of SC changes from the interaction-energy origin to the kinetic-energy origin.[8]

5.2 Pair correlation function

To directly confirm the appearance of $d_{x^2-y^2}$-wave SC, the d-wave nearest-neighbor pair correlation function $P_d(\mathbf{r})$ is convenient for the present approach:[60]

$$P_d(\mathbf{r}) = \frac{1}{N_s} \sum_i \sum_{\tau,\tau'=\hat{\mathbf{x}},\hat{\mathbf{y}}} (-1)^{1-\delta(\tau,\tau')}$$
$$\times \left\langle \Delta_\tau^\dagger(\mathbf{R}_i) \Delta_{\tau'}(\mathbf{R}_i + \mathbf{r}) \right\rangle, \quad (21)$$

where $\hat{\mathbf{x}}$ and $\hat{\mathbf{y}}$ denote the lattice vectors in the x- and y-directions, respectively, and $\Delta_\tau^\dagger(\mathbf{R}_i)$ is the creation operator of a nearest-neighbor singlet,

$$\Delta_\tau^\dagger(\mathbf{R}_i) = (c_{i\uparrow}^\dagger c_{i+\tau\downarrow}^\dagger + c_{i+\tau\uparrow}^\dagger c_{i\downarrow}^\dagger)/\sqrt{2}. \quad (22)$$

If $P_d(\mathbf{r})$ has a finite value for $|\mathbf{r}| \to \infty$, off-diagonal long-range order exists. For finite systems, however, we have to appropriately determine long-distance values of $P_d(\mathbf{r})$, particularly, in the cases of small U/t, where the correlation length is long. In Fig. 23, $P_d(\mathbf{r})$ is plotted for two values of t'/t. Although $P_d(\mathbf{r})$ for large $|\mathbf{r}|$ should vanish for $U/t = 0$, spikes of sizable magnitude appear near $\mathbf{r} = (L/2, L/2)$ $[(0, L/2)]$ for $t'/t = 0$ $[-0.4]$ for this system size.[61] Furthermore, a trace of this spike structure remains up to fairly large values of U/t. Thus, for small U/t, we should choose $P_d(\mathbf{r})$ which does not have such peculiar finite-sized effects. Fortunately, we found that, in the noninteracting cases, the magnitude of $|P_d(\mathbf{r})|$ for $\mathbf{r} = (L/2 - 1, L/2)$, which is almost the farthermost point, is very small (less than 10^{-4}) for arbitrary values of t'/t and L. Hence, we employ $P_d[(L/2 - 1, L/2)]$ as the large-$|\mathbf{r}|$ value, P_d^∞, for small U/t, namely, $0 \le U \le U_{\mathrm{max}}$, with U_{max} being the value at which $P_d(\mathbf{r})$ becomes maximum. For the strong-correlation regime $(U > U_{\mathrm{max}})$, $P_d(\mathbf{r})$ becomes almost constant for $|\mathbf{r}| \ge 3$,[62,63] as shown in Fig. 23. Hence, in this regime, we adopt the average of $P_d(\mathbf{r})$ for $|\mathbf{r}| \ge 3$ as P_d^∞.
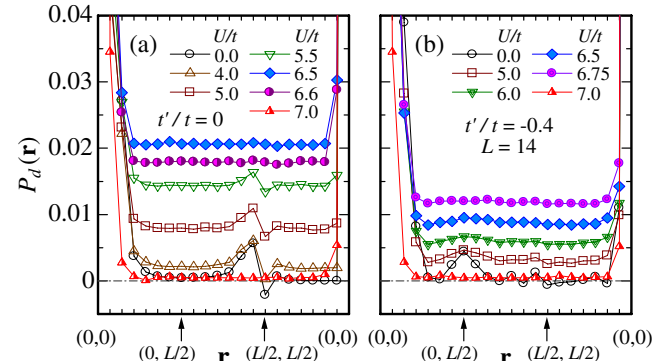

Fig. 23. (Color online) Real-space pair correlation function of d-wave symmetry along path of $\mathbf{r}$, $(0,0)$–$(0,L/2)$–$(L/2,L/2)$–$(0,0)$, for various values of U/t. (a) $t'/t = 0$ and (b) $t'/t = -0.4$, both for $L = 14$. The scale of the ordinate axis is common to both panels. The data are obtained, using VMC calculations for $U \ne 0$, and from the analytic formula for $U = 0$.

In Figs. 24(a) and 24(b), P_d^∞ thus obtained is plotted as a function of U/t. In the weakly correlated regime $(U/t \lesssim 4)$, the increase in P_d^∞ is small, irrespective of the value of t'/t. For weakly frustrated cases $(|t'/t| \lesssim 0.3)$, P_d^∞ starts to increases appreciably at $U \sim U_{\mathrm{onset}}$ as U/t increases, has a peak at $U/t = 6$–6.25, and then abruptly decreases at the Mott critical point $U = U_c$. The system-size dependence of P_d^∞ near the peak is weak for $L \ge 12$. Thus, in these cases, robust d-wave SC certainly occurs for $U_{\mathrm{onset}} \lesssim U < U_c$. On the other hand, for strongly frustrated cases $[|t'/t| \gtrsim 0.4$ in Fig. 24(b)], no sizable increase in P_d^∞ is observed at the value corresponding to U_{onset}. P_d^∞ slowly and monotonically increases until it abruptly drops at $U = U_c$.[59] Moreover, the system-size dependence is very large. Eventually, robust d-wave SC occurs in a limited area, $U_{\mathrm{onset}} \lesssim U < U_c$ and $|t'/t| \lesssim 0.3$, within Ψ_Q^d. A similar result has been recently obtained using a fluctuation exchange approximation.[64]

In Fig. 24(c), we show the magnification of P_d^∞ near the Mott critical points. In the insulating regime $(U > U_c)$, P_d^∞ becomes almost independent of t'/t, as mentioned in item (5) in §3.3, decreases rapidly as the system size L increases, and probably vanishes in the limit of $L \to \infty$. Because the
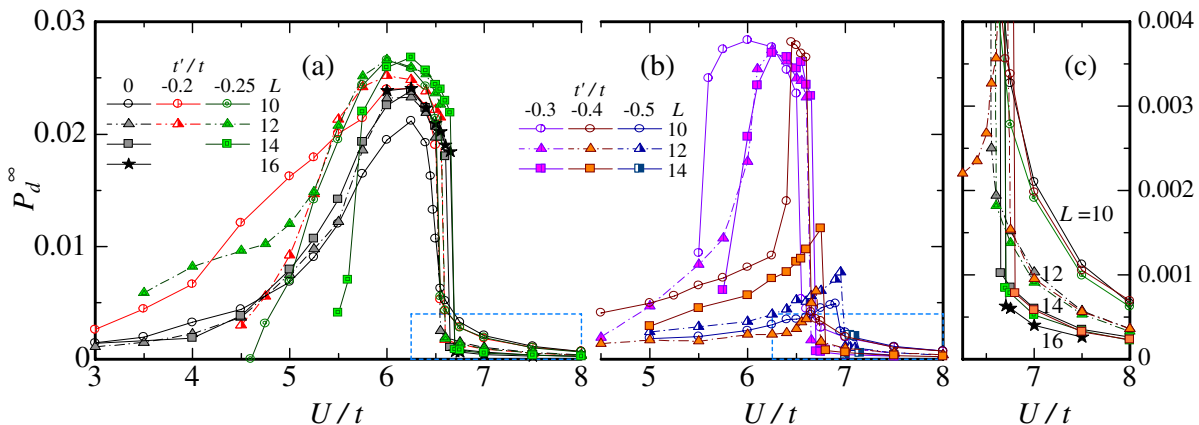

Fig. 24. (Color online) Large-$|\mathbf{r}|$ value of d-wave pair correlation function $P_d(\mathbf{r})$ for (a) small $|t'/t|$ (≤ 0.25) and (b) large $|t'/t|$ (≥ 0.3). Data of various system sizes for each value of t'/t are plotted. (c) Magnification of P_d^∞ near the Mott critical points. The data for only $t'/t = 0$, -0.25, and -0.4 are shown for clarity. The range of (c) is indicated by a dashed-line boxes in (a) and (b).
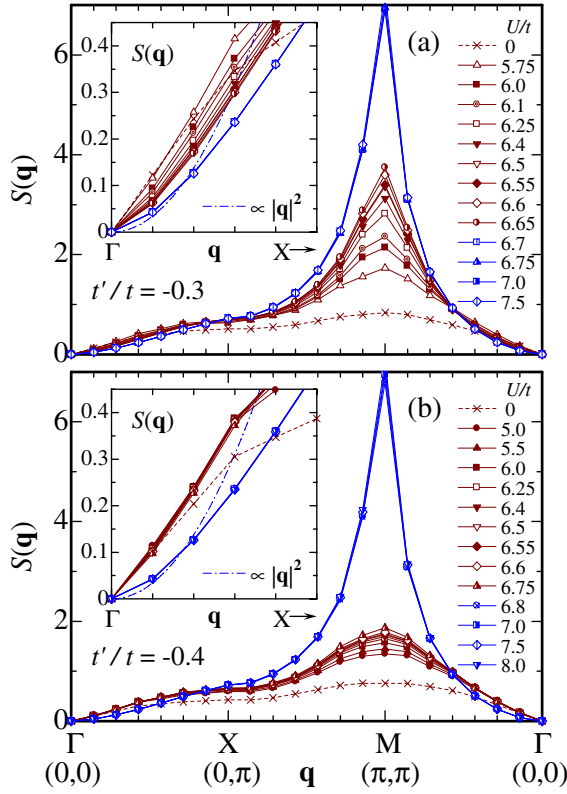
Fig. 25. (Color online) Spin structure factor for (a) $t'/t = -0.3$ [$U_c/t = 6.69$] and (b) $t'/t = -0.4$ [$U_c/t = 6.78$] for various U near U_c in Ψ_Q^d. The system size is $L = 14$. The insets show the magnification of the region near the Γ point on the Γ–X line, and the symbols are common to the main panel. Data points of different Us for $U > U_c$ almost overlap one another. Similar data for $t'/t = 0$ are given in Fig. 14.

statistical fluctuation in the VMC data is much smaller in the insulating regime than in the conductive regime, the data are more reliable. The disappearance of P_d^∞ for $U > U_c$ is expected in an insulating state.

5.3   Properties of superconductivity

First, we study the relation between d-wave SC and AF correlation. In Figs. 14, 25(a), and 25(b), the U/t dependence of $S(\mathbf{q})$ in Ψ_Q^d is shown for $t'/t = 0$, -0.3, and -0.4, respectively. As mentioned, robust SC arises for $t'/t = 0$ and -0.3, but does not for $t'/t = -0.4$ (Fig. 24). This is supported by the small-$|\mathbf{q}|$ behavior of $S(\mathbf{q})$, shown in the insets of Fig. 25. For $t'/t = -0.3$, $S(\mathbf{q})$ for small $|\mathbf{q}|$ tends to be quadratic in $|\mathbf{q}|$ as U/t increases, indicating that a SC gap develops, whereas for $t'/t = -0.4$, $S(\mathbf{q})$ remains almost linear in $|\mathbf{q}|$.

We now focus on the AF wave number $\mathbf{G}$. For $U = 0$, $S(\mathbf{q})$ has a pointed peak for $t' = 0$, a rounded peak for $t'/t = -0.3$ and a flat top for -0.4, due to the frustration. For the cases of $t'/t = 0$ and -0.3, in which robust SC appears, $S(\mathbf{G})$ steadily increases as U/t increases, even in the conductive regime, $U < U_c$ [Figs. 14 and 25(a)]. In the strongly frustrated case ($t'/t = -0.4$), in which the SC correlation does not develop, the magnitude of $S(\mathbf{G})$ reaches no more than half that for $t'/t = -0.3$, although $S(\mathbf{q})$ increases slightly for $U < U_c$ [Fig. 25(b)]. To consider the t'/t dependence of $S(\mathbf{q})$ explicitly, we plot $S(\mathbf{q})$ for various values of t'/t in Fig. 26(a) at $U/t = 6$, near which P_d^∞ has a
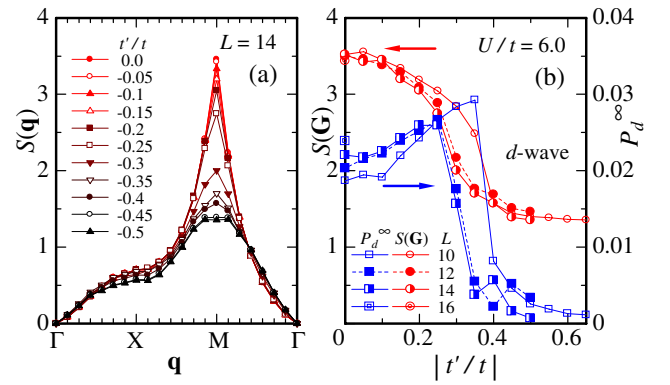

Fig. 26. (Color online) (a) t'/t dependence of spin structure factor for $U/t = 6$, where P_d^∞ is considerably enhanced particularly for small t'/t. (b) Spin structure factor at the AF wave number $\mathbf{G}$ for $U/t = 6$ as a function of t'/t is denoted by circles (left axis). Simultaneously, the d-wave pair correlation function is plotted with squares (right axis).
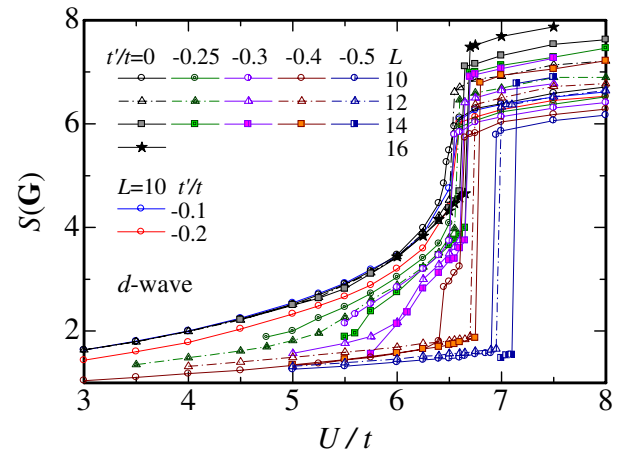

Fig. 27. (Color online) U/t dependence of spin structure factor at AF wave number $\mathbf{G}$ for various values of t'/t and L.

maximum (see Fig. 24). When t'/t is varied, the change in $S(\mathbf{q})$ is quantitatively insignificant, except near the M point. As $|t'/t|$ increases, $S(\mathbf{G})$ sharply decreases, particularly at $t'/t \sim -0.3$, and $\mathbf{G}$ is no longer a characteristic wave number for $|t'/t| \gtrsim -0.45$. In Fig. 26(b), we compare the t'/t dependence of $S(\mathbf{G})$ with that of P_d^∞. In respective system sizes, when $S(\mathbf{G})$ abruptly decreases for $|t'/t| > 0.25$, P_d^∞ similarly decreases. In Fig. 27, we show the U/t dependence of $S(\mathbf{G})$. Although in every case $S(\mathbf{G})$ generally increases as U/t increases, the range of significant increase [$S(\mathbf{G}) \gtrsim 2$] in the conductive regime roughly corresponds to $U_\mathrm{onset} \lesssim U < U_c$, and is accompanied by a marked increase in P_d^∞ (Fig. 24). We have confirmed, for a wide range of model parameters, that whenever P_d^∞ is appreciably enhanced, $S(\mathbf{q})$ has an evident peak at $\mathbf{q} = \mathbf{G}$. This result strongly supports the idea that the SC in this model is induced by AF spin correlation. Incidentally, this mechanism is reflected in the ratio of energy components. As shown in Table III ($U/t = 6.25$), when SC is weak ($|t'/t| = 0.4$), ρ is only slightly smaller than the noninteracting value, whereas for robust SC ($|t'/t| = 0.25$), ρ becomes less than half the value for $U = 0$; the diagonal hopping is considerably suppressed.
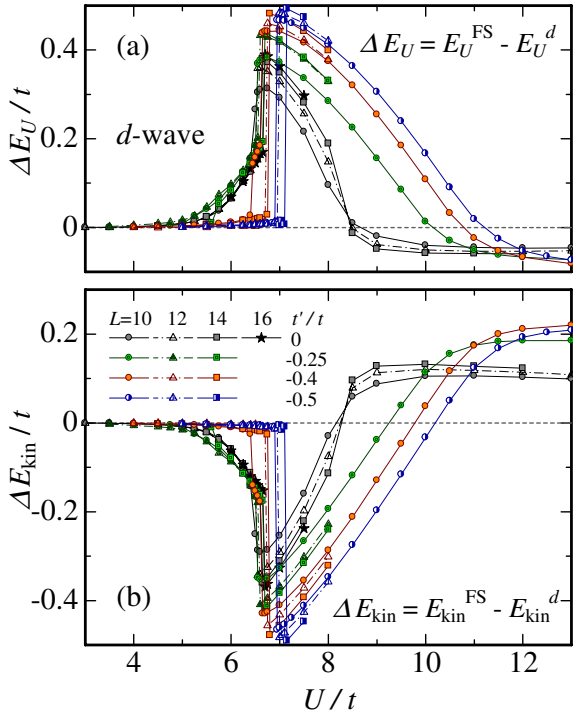
Fig. 28. (Color online) (a) Interaction and (b) kinetic components of condensation energy due to Ψ_Q^d as a function of interaction strength for four values of t'/t. Various system sizes are plotted. The symbols and scales are common to both panels.

Fig. 29. (Color online) (a) Comparison of the condensation energy for $t'/t = 0$ among Ψ_Q^d (indicated by Q/d), Ψ_Q^{AF} (Q/AF) and $\mathcal{P}_G\Phi_d$ (G/d), for which $\Delta E = E(\mathcal{P}_G\Phi_{FS}) - E(\mathcal{P}_G\Phi_d)$. Several system sizes are plotted to consider the L dependence. (b) Kinetic (closed symbols) and interaction (open symbols) parts of the condensation energy due to Ψ_Q^{AF} for $t'/t = 0$. Four system sizes are used.

Fig. 30. (Color online) Ground-state phase diagram in t'–U space constructed from VMC calculations performed in this study. The abbreviations AF-I, P-I (P-M) and SC denote AF insulator, paramagnetic insulator (metal) and superconductor, respectively.

Next, we consider the energy gain in the SC transition. The components of condensation energy are shown in Fig. 28, that is, the differences in kinetic and interaction energies between Ψ_Q^d and Ψ_Q^{FS}; the actual expression is given in the figure. Here, $E_{kin} = \langle \mathcal{H}_{kin} \rangle = E_t + E_{t'}$, and $\Delta E_{kin} + \Delta E_U = \Delta E \ (\geq 0)$ [eq. (20)]. In the SC regime ($U < U_c$), ΔE_{int} (ΔE_{kin}) is always positive (negative), regardless of the value of t'/t. This indicates that the SC transition is induced by the gain in the interaction energy at the expense of kinetic energy. This feature smoothly continues to the weak-coupling limit ($U/t \to 0$), and is common to conventional BCS superconductors. Although the component of energy gain switches to the kinetic energy at $U = 8t$–$11t$, which broadly corresponds to U_c^{FS}, SC is excluded for $U > U_c$. The kinetic-energy-driven SC is not realized at half filling, in contrast to that in the doped cases.[8]

Incidentally, this behavior of ΔE_{kin} and ΔE_U is not restricted to the d-wave state, but is also found in some order–disorder transitions. As an example, we plot, in Fig. 29(b), ΔE_{kin} ($= \Delta E_t$) and ΔE_U for the AF state Ψ_Q^{AF} [eq. (14)], which will be discussed in the next section, for $t'/t = 0$. The interaction part ΔE_U makes a positive contribution to ΔE for $U/t \lesssim 8$, whereas the kinetic part ΔE_t contributes for $U/t \gtrsim 7$. Hence, the behavior is qualitatively identical to that of Ψ_Q^d. Such behavior is also observed in SC and CDW states for the two-dimensional attractive Hubbard model.[65]

6. Phase Diagram and Antiferromagnetism

Up to this point, we have not considered the competition with the AF state, but it is a crucial problem when drawing a phase diagram. We thus compare the stability between Ψ_Q^d
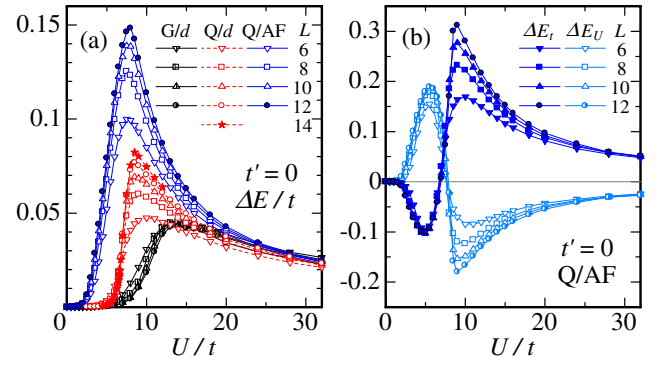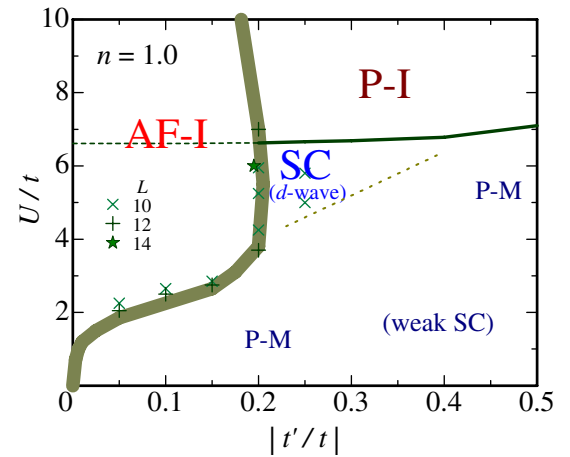
and the AF-ordered state Ψ_Q^{AF} [eq. (14)] into which we do not introduce band renormalization parameters to equalize the condition with Ψ_Q^d. Whenever Δ_{AF} is finite at half filling, Ψ_Q^{AF} is insulating and has an AF long-range order; the sublattice magnetization m [eq. (19)] behaves similarly to Δ_{AF}.

In Fig. 30, we show a phase diagram constructed as follows. The boundary between AF-I and P-M ($|t'/t| \leq 0.2$) is determined by the points where the extrapolated values of Δ_{AF} vanish. The boundary between AF-I and SC (or P-I) is determined by the comparison of the total energies. The boundary between P-I and P-M is determined by U_c/t for the largest systems for each t'/t obtained in §3. The last boundary is extended to $t'/t = 0$ if Ψ_Q^{AF} is not allowed, as indicated by a dashed line. It is unnecessary to fix the boundary between SC and P-M, because the small magnitude of Δ often survives for extremely small U/t; instead, we show U_{onset}/t with a dotted line.

For $t'/t = 0$, a continuous metal-to-AF-insulator transition occurs at $U = U_c^{AF} = 0$,[14] owing to the complete nesting condition. This AF state is very stable and continues to the

Heisenberg limit ($U/t \to \infty$). Our result is consistent with it, as shown in Fig. 29(a), where the condensation energy for Ψ_Q^{AF} is always larger than that for Ψ_Q^d. The nature of the continuous transition seems to be preserved in the region of small $|t'/t|$, although U_c^{AF} becomes finite, and the tendency toward a first-order transition gradually develops as $|t'/t|$ increases. Note that as the frustration becomes strong, Ψ_Q^{AF} is rapidly destabilized, and surrenders to Ψ_Q^d at $t' = t_c' \sim -0.2t$. Moreover, $|t_c'/t|$ tends to decrease as U/t increases; this feature is consistent with the result that the AF state has the largest range of n at $U \sim W$ in a phase diagram in the n–U plane.[8] However, this tendency is not in accord with the arguments of the J–J' spin model, which is an effective model of eq. (1) for large U/t. Various studies of the J–J' model[66] concluded that the AF order vanishes at much larger values: $J'/J \sim 0.4$ ($|t'/t| \sim 0.63$).

We consider that this discrepancy is primarily due to the choice of variational states: (1) Ψ_Q^d does not have a seed of AF long-range order, although the AF short-range correlation appreciably develops, and (2) in Ψ_Q^{AF}, we have not allowed for the band renormalization effect. These two requirements are satisfied simultaneously by adopting a coexisting state of AF and SC gaps,[67,68] with a band renormalization effect.[46] In fact, we have performed VMC calculations using such a wave function for the anisotropic triangular lattice and found that the area of the AF phase considerably expands.[69] A similar result has been obtained independently by Chen,[70] and also for the checkerboard lattice by Koga *et al.*[41] Thus, it is urgent that the wave function is improved in this line to refine the phase diagram.

7. Conclusions

7.1 Summary

Using an optimization variational Monte Carlo method, we have studied the half-filled-band Hubbard model on frustrated square lattices, given by eq. (1). Our primary aim is to understand the mechanisms of the Mott transition and of the $d_{x^2-y^2}$-wave SC arising in the Hubbard model. To this end, we introduce an intersite correlation factor that controls the binding between a doublon and a holon into the trial functions: normal (Fermi sea), d-wave singlet and AF states. We have succeeded in describing the d-wave SC and a Mott transition simultaneously in a single approach. We itemize our main findings:

(1) Within the d-wave singlet state, a first-order Mott (conductor-to-nonmagnetic-insulator) transition occurs at U_c, which is approximately the bandwidth, for arbitrary t'/t. In the insulating regime, most doublon–holon pairs are actually confined within the nearest-neighbor sites, in contrast to the case in the conductive regime. The critical U_c/t gradually increases as the frustration becomes strong. This transition is not directly related to a magnetic order.

(2) We have confirmed that in the projected Fermi sea, a first-order Mott transition without relevance to magnetism also arises at a larger U/t than the bandwidth for arbitrary t'/t, although the state does not have the lowest energy.

(3) The nonmagnetic insulating state (d-wave singlet state for $U > U_c$) has a considerably low energy and a strong short-range AF correlation. According to the

small-$|\mathbf{q}|$ behavior of $S(\mathbf{q})$, the d-wave state tends to have short singlet bonds owing to the nearest-neighbor pairing [eq. (12)], in contrast to the projected Fermi sea, which clearly does not have a spin gap.

(4) Robust SC with $d_{x^2-y^2}$-wave symmetry appears for moderate values of U/t (~ 6) and t'/t ($0.2 \lesssim |t'/t| \lesssim 0.35$). This area is adjacent to both domains of a Mott insulator and an AF long-range order. The phase diagram obtained in this study is shown in Fig. 30.

(5) By comparing the pair correlation function with $S(\mathbf{q})$, it is found that robust SC is always accompanied by appreciably enhanced short-range AF spin correlation, which is weakened by the frustration and almost vanishes for $|t'/t| \gtrsim 0.35$. The SC transition is induced by the gain in interaction energy; this mechanism is identical to that in the weak-correlation limit as well as that of conventional BCS superconductors.

(6) The AF long-range order prevailing in the weakly frustrated cases ($|t'/t| \lesssim 0.2$) is rapidly destabilized as $|t'/t|$ increases if a band renormalization effect is not introduced.

7.2 Further discussions

(1) In comparing the present study for the frustrated square lattice [Fig. 1(a)] with the preceding study,[6] in which almost the same wave functions are applied to the anisotropic triangular lattice [Fig. 1(b)], the results for the two lattices are qualitatively identical, indicating that the two types of frustration work similarly unless $|t'/t|$ is too large. However, the critical values with respect to t'/t are approximately doubled for the latter lattice; namely, the AF state becomes unstable at approximately $|t'/t| = 0.2$ for the former and 0.4 for the latter, and the robust SC disappears at approximately $|t'/t| = 0.35$ for the former, and 0.8 for the latter. This can be explained by the difference in the number of frustrated bonds.

(2) Recently, using a VMC method with a two-body long-range Jastrow factor for the square lattice ($t' = 0$), Capello *et al.*[71] found that a metal-to-insulator transition arises, similar to that in Ψ_Q^{FS}, for example, in the behavior of Z and d. The critical value of their function is $U_c/t \sim 8.5$, which is close to 8.73 ($L = 18$) in Ψ_Q^{FS}. Although their transition is regarded as continuous, evidence of the first order is possibly be found by a detailed analysis of larger systems. In their wave function, no explicit (four-body) doublon–holon binding factor is introduced, but a short-range part of the two-body Jastrow factor may substantially work as a binding factor under the condition of strong electron repulsion at half filling. It will be interesting to reveal the relation between the two wave functions.

(3) In this paper, we have restricted the electron density to half filling ($n = 1$). When carriers are doped, unless the doping rate $|1 - n|$ is too large, the doublon–holon-binding effect remains significant, as we showed for $t' = 0$ in the previous letter.[8] The Mott transition at half filling changes to a crossover from weakly to strongly correlated regimes. As $|1 - n|$ increases, the AF order is rapidly destabilized, and the SC phase

expands to the region of large U/t, consistent with the behavior of high-T_c cuprates. We will report a detailed description of doped cases with the effect of frustration elsewhere.

Acknowledgments

1) K. Kanoda: Physica C **282–287** (1997) 299; K. Miyagawa, K. Kanoda and A. Kawamoto: Chem. Rev. **104** (2004) 5635; R. H. McKenzie: Science **278** (1997) 820.
2) H. Kino and H. Fukuyama: J. Phys. Soc. Jpn. **65** (1996) 2158.
3) A. Tsukada, Y. Krockenberger, M. Noda, H. Yamamoto, D. Manske, L. Alff and M. Naito: Solid State Commun. **133** (2005) 427.
4) C. J. Umrigar, K. G. Wilson and J. W. Wilkins: Phys. Rev. Lett. **60** (1988) 1719.
5) For example, C. J. Umrigar and C. Filippi: Phys. Rev. Lett. **94** (2005) 150201; S. Sorella: Phys. Rev. B **71** (2005) 241103.
6) T. Watanabe, H. Yokoyama, Y. Tanaka and J. Inoue: J. Phys. Soc. Jpn. **75** (2006) 074707.
7) B. Bernu, P. Lecheminant, C. Lhuillier and L. Pierre: Phys. Rev. B **50** (1994) 10048; L. Capriotti, A. E. Trumper and S. Sorella: Phys. Rev. Lett. **82** (1999) 3899.
8) H. Yokoyama, Y. Tanaka, M. Ogata and H. Tsuchiura: J. Phys. Soc. Jpn. **73** (2004) 1119.
9) J. Hubbard: Proc. R. Soc. London, Ser. A **276** (1963) 237.
10) J. Kanamori: Prog. Theor. Phys. **30** (1963) 275.
11) M. C. Gutzwiller: Phys. Rev. Lett. **10** (1963) 159.
12) P. W. Anderson: Science **235** (1987) 1196.
13) For example, T. Tanamoto, H. Kohno and H. Fukuyama: J. Phys. Soc. Jpn. **61** (1992) 1886; T. Tohyama and S. Maekawa: Phys. Rev. B **49** (1994) 3596; R. Raimondi, J. H. Jefferson and L. F. Feiner: Phys. Rev. B **53** (1996) 8774; E. Pavarini, I. Dasgupta, T. Saha-Dasgupta, O. Jepsen and O. K. Anderson: Phys. Rev. Lett. **87** (2001) 047003.
14) For example, J. E. Hirsch: Phys. Rev. B **31** (1985) 4403.
15) H. Kondo and T. Moriya: J. Phys. Soc. Jpn. **65** (1996) 2559; H. Kondo and T. Moriya: J. Phys. Soc. Jpn. **67** (1998) 234.
16) R. Chitra and G. Kotliar: Phys. Rev. Lett. **83** (1999) 2386; T. Pruschke: *Proc. Yukawa Int. Seminar 2004 (YKIS 2004)*, Prog. Theor. Phys. Suppl. No. 160 (2005) 274.
17) T. Kashima and M. Imada: J. Phys. Soc. Jpn. **70** (2001) 3052.
18) T. Mizusaki and M. Imada: Phys. Rev. B **74** (2006) 014421.
19) For example, B. Kyung and A.-M. S. Tremblay: Phys. Rev. Lett. **97** (2006) 046402, and references therein.
20) R. Jastrow: Phys. Rev. **98** (1955) 1479.
21) M. C. Gutzwiller: Phys. Rev. **137** (1965) A1726.
22) For a review, D. Vollhardt: Rev. Mod. Phys. **56** (1984) 99.
23) W. L. McMillan: Phys. Rev. **138** (1965) A442; D. Ceperley, G. V. Chester and K. H. Kalos: Phys. Rev. B **16** (1977) 3081.
24) H. Yokoyama and H. Shiba: J. Phys. Soc. Jpn. **56** (1987) 1490.
25) C. Gros, R. Joynt and T. M. Rice: Phys. Rev. B **36** (1987) 381.
26) W. Metzner and D. Vollhardt: Phys. Rev. B **37** (1988) 7382; F. Gebhard and D. Vollhardt: Phys. Rev. B **38** (1988) 6911.
27) H. Yokoyama and H. Shiba: J. Phys. Soc. Jpn. **59** (1990) 3669.
28) C. Castellani, C. Di Castro, D. Feinberg and J. Ranninger: Phys. Rev. Lett. **43** (1979) 1957.
29) T. A. Kaplan, P. Horsch and P. Fulde: Phys. Rev. Lett. **49** (1982) 889; see also, P. Fazekas: Phys. Scr. T **29** (1989) 125.
30) E. H. Lieb and F. Y. Wu: Phys. Rev. Lett. **21** (1968) 192.
31) H. Yokoyama and M. Ogata: Phys. Rev. Lett. **67** (1991) 3610; H. Yokoyama and M. Ogata: Phys. Rev. B **53** (1996) 5758.
32) H. Yokoyama and H. Shiba: J. Phys. Soc. Jpn. **57** (1988) 2482.
33) C. Gros: Ann. Phys. (N.Y.) **189** (1989) 53.
34) H. Yokoyama and M. Ogata: J. Phys. Soc. Jpn. **65** (1996) 3615.
35) Here, S is explicitly given by

$$\sum_{\langle ij \rangle \sigma} \frac{-\mathrm{i}t}{U} \left[n_{i-\sigma}(1 - n_{j-\sigma})c_{i\sigma}^{\dagger}c_{j\sigma} - n_{j-\sigma}(1 - n_{i-\sigma})c_{i\sigma}^{\dagger}c_{j\sigma} \right].$$

For sufficiently large U/t and $n \sim 1$, one may expand $e^{\mathrm{i}S}$, and keep only essential $(t$–$J)$ terms of the order t^2/U, in addition to the zeroth-order terms. See, A. B. Harris and R. V. Lange: Phys. Rev. **157** (1967) 295.
36) H. Otsuka: J. Phys. Soc. Jpn. **61** (1992) 1645.
37) A. J. Millis and S. N. Coppersmith: Phys. Rev. B **43** (1991) 13770.
38) H. Yokoyama: Prog. Theor. Phys. **108** (2002) 59.
39) In the results of ref. 27, Ψ_q^{FS}, even in one dimension, seems to induce a Mott transition between $U/t = 4$ and 16. We speculate that a longer-range doublon–holon binding factor is crucial in one dimension to reduce U_c down to zero.
40) S. Kuratani, A. Koga and N. Kawakami: private communication.
41) A. Koga, T. Yoshioka, N. Kawakami and H. Yokoyama: submitted to J. Magn. Magn. Mater. and Physica C.
42) A. Koga, N. Kawakami, H. Yokoyama and K. Kobayashi: to be published in Proc. LT24.
43) J. P. Bouchaud, A. Georges and C. Lhuillier: J. Phys. (Paris) **49** (1988) 553.
44) H. Yoshimura and D. S. Hirashima: J. Phys. Soc. Jpn. **74** (2005) 712; T. Watanabe, T. Miyata, H. Yokoyama, Y. Tanaka and J. Inoue: J. Phys. Soc. Jpn. **74** (2005) 1942.
45) F. C. Zhang, C. Gros, T. M. Rice and H. Shiba: Supercond. Sci. Technol. **1** (1988) 36.
46) A. Himeda and M. Ogata: Phys. Rev. Lett. **85** (2000) 4345.
47) H. Shiba: Prog. Theor. Phys. **48** (1972) 2171; Y. Nagaoka: Prog. Theor. Phys. **52** (1974) 1716.
48) H. Yokoyama and H. Shiba: J. Phys. Soc. Jpn. **56** (1987) 3582.
49) For example, K. Kobayashi and K. Iguchi: Phys. Rev. B **47** (1993) 1775.
50) W. H. Press, S. A. Teukolsky, W. T. Vetterling and B. P. Flannery: *Numerical Recipes in FORTRAN* (Cambridge, New York, 1992) 2nd ed., p. 406.
51) In the present VMC procedure, if the energy barrier between the two local energy minima is sufficiently high, the optimized variational parameters are trapped in the local minima to which the initial parameter values tend. Thus, as seen in Figs. 3, 5, and 6, we can obtain the optimized values for both local minima by giving the respective initial parameters anticipated from those obtained for nearby data points. On the other hand, if the barrier becomes as low as the statistical fluctuation in E/t (we assume there are still two energy minima), the parameters readily arrive at the global minima, jumping over the barrier. Therefore, it is not easy to determine the values of U/t at which the double-minimum structure of E/t vanishes, namely, to draw the accurate hysteresis curves.
52) The data of μ for $L = 8$–16 seems fitted well with a linear function of N_s^{-1} $(= L^{-2})$. Thereby, we estimated approximate values of μ for $L = \infty$ and $t' = 0$ as $\mu = 0.912$–0.945 for $U/t = 6.75$–10; as U/t increases, μ tends to increase.
53) W. F. Brinkman and T. M. Rice: Phys. Rev. B **2** (1970) 4302.
54) M. J. Rozenberg, R. Chitra and G. Kotliar: Phys. Rev. Lett. **83** (1999) 3498.
55) The behavior of $n(\mathbf{k})$ for finite values of t'/t is basically the same. In some cases, however, the position of the (quasi) Fermi surface moves as U/t increases and crosses a discrete $\mathbf{k}$-point of the finite system. Then, it becomes difficult to accurately determine the values of Z as a function of U/t, because the position of the Fermi surface is not specified. For instance, the case of $t'/t = -0.25$ and $L = 14$ exhibits such inconvenient behavior.
56) In ref. 6, the optimized chemical potential ζ is positive, because the sign of t'/t is assumed positive, contrary to the present case. The behavior of $|\zeta|$ for $U < U_c$ in ref. 6 is broadly similar to that in Fig. 4(e), whereas for $U > U_c$, ζ decreases to nearly zero, which is the value for $t'/t = 0$, but never becomes negative.
57) R. Bulla: Phys. Rev. Lett. **83** (1999) 136.
58) Y. Shimizu, K. Miyagawa, K. Kanoda, M. Maesato and G. Saito: Phys. Rev. Lett. **91** (2003) 107001.
59) For $6.4 \lesssim U/t < 6.64$ $(= U_c/t)$, Ψ_Q^d with $t'/t = -0.4$ and $L = 10$ has a special $\mathbf{k}$-point configuration [observed in $n(\mathbf{k})$ (not shown)], which

is different from the cases of $U/t \leq 6.4$, and is advantageous to SC. One finds in Fig. 4 that each of the optimized parameters for $t'/t = -0.4$ and $L = 10$ has a value similar to that which induces SC (e.g., $|t'/t| \leq 0.3$) only for $6.4 \lesssim U/t < 6.64$. Correspondingly, $P_d(\mathbf{r})$ shown in Fig. 24(b) has extremely large values for the above values of U/t. This enhancement of SC is spurious, because there is no such remarkable behavior for $L = 12$ and 14. Such behavior sometimes appears near the critical value of t'/t, where predominant SC vanishes, and for specific system sizes, boundary conditions and model parameters. Also at this point, we need to check the system-size dependence.

60) When U/t is small and the coherence length is long, one needs to consider the SC correlation functions of longer Cooper pairs. In the present study, however, $P_d(\mathbf{r})$ in eq. (21) is useful, because we are interested in the occurrence of SC, particularly, near the Mott transition.

61) As L is increased, the magnitude of spikes gradually decreases. We need to use the systems of $L = 30$–50 in which the spikes for $U/t = 0$ appear negligible on the scale of Fig. 23.

62) C. T. Shih, T. K. Lee, R. Eder, C.-Y. Mou and Y. C. Chen: Phys. Rev. Lett. **92** (2004) 227002.

63) We adopt the Manhattan metric to measure $|\mathbf{R}|$ and $|\mathbf{r}|$.

64) S. Onari, H. Yokoyama and Y. Tanaka: in preparation.

65) H. Yokoyama: unpublished.

66) L. Spanu and A. Parola: Phys. Rev. B **72** (2005) 174418; L. Capriotti and S. Sorella: Phys. Rev. Lett. **84** (2000) 3173; J. Oitmaa and W. Zheng: Phys. Rev. B **54** (1996) 3022; J. Igarashi: J. Phys. Soc. Jpn. **62** (1993) 4449; T. Nakamura and N. Hatano: J. Phys. Soc. Jpn. **62** (1993) 3062; J. H. Xu and C. S. Ting: Phys. Rev. B **42** (1990) 6861.

67) T. Giamarchi and C. Lhuillier: Phys. Rev. B **43** (1991) 12943.

68) A. Himeda and M. Ogata: Phys. Rev. B **60** (1999) 9935.

69) T. Watanabe, H. Yokoyama, Y. Tanaka and J. Inoue: submitted to J. Magn. Magn. Mater., and in preparation.

70) Y. C. Chen: private communication.

71) M. Capello, F. Becca, S. Yunoki and S. Sorella: Phys. Rev. B **73** (2006) 245116.